

# Hydrothermal fluid evolution in collisional Miocene porphyry copper deposits in Iran: Insights into factors controlling metal fertility

Alireza Zarasvandi<sup>a,\*</sup>, Mohsen Rezaei<sup>a</sup>, Johann G. Raith<sup>b</sup>, Sina Asadi<sup>c</sup>, David Lentz<sup>d</sup>

<sup>a</sup> Department of Geology, Faculty of Earth Science, Shahid Chamran University of Ahvaz, Ahvaz, Iran

<sup>b</sup> Department of Applied Geosciences and Geophysics, Montanuniversität Leoben, Leoben, Austria

<sup>c</sup> Department of Earth Sciences, Faculty of Sciences, Shiraz University, Shiraz, Iran

<sup>d</sup> Department of Earth Sciences, University of New Brunswick, Fredericton, NB, Canada

## ARTICLE INFO

### Keywords:

Fluid inclusion  
Laser Raman spectroscopy  
Hydrothermal fluids  
Porphyry copper system  
Urumieh-Dokhtar Magmatic Belt  
Iran

## ABSTRACT

The Cenozoic Urumieh-Dokhtar Magmatic Belt (UDMB) in Iran is considered as one of the major Cu-bearing regions in the world with high potential for the occurrence of giant/large porphyry Cu  $\pm$  Mo  $\pm$  Au systems. In the UDMB, porphyry Cu mineralization is strictly associated with Miocene intrusions originating mostly from collisional-related partial melting of subduction-modified juvenile lower crust. In this study fluid inclusion coupled with laser Raman analysis is used to characterize and compare the fluid evolution of the large Meiduk deposit and smaller low grade porphyry copper systems (e.g., Keder, Sarkuh, and Iju) in the UDMB. It can be shown that enhancement of metal fertility of a porphyry system is controlled by several factors: (1) The salinity of early hydrothermal ore fluids; maximum ore-efficiency is seen in porphyry deposits showing supersaturation of NaCl in the pristine high temperature fluids (e.g., Meiduk), (2) Presence of CO<sub>2</sub> and fast exhausting of CO<sub>2</sub> vapor components during early stages of mineralization, (3) Temperature decrease especially during the main ore stage, and (4) High oxygen fugacity (near to the magnetite – hematite oxygen buffer) of the most primitive fluids in the early stages of hydrothermal system.

## 1. Introduction

Porphyry Cu  $\pm$  Mo  $\pm$  Au deposits likely are the best studied ore systems and they provide most of the world's Cu and Mo reserves (~80% Cu and ~95% Mo; e.g., Sillitoe, 2010; Sun et al., 2015; Blundy et al., 2015; Richards, 2015b; Chelle-Michou et al., 2017). These deposits are typically associated with high temperature magmatic-hydrothermal systems (300–700 °C) that originated mostly from shallowly emplaced metal-rich oxidized magmas in subduction and/or collisional as well as post-collisional tectonic settings (Richards, 2011, 2013, 2015a,b). Aside from magma generation by partial melting of the metasomatized mantle wedge in normal arc setting, it is now accepted that the generation of porphyry magmas may also be related to the melting of subduction-modified subcontinental lithospheric mantle or melting of orogenically thickened lower crust, and when there is asthenosphere upwelling especially in collided plate margins (e.g., Richards, 2015b). Excellent examples of the latter are found in the Tethyan orogenic belt, where there are several separate collided arcs hosting a wide variety of porphyry and epithermal systems (Richards, 2015a,b). In Iran, the UDMB as part of the Zagros orogen is one segment in the western

Tethyan realm. In this belt, the most important porphyry copper deposits (PCD) are related to collisional high Sr/Y Miocene adakite-like porphyry intrusions and not to Eocene-Oligocene pre-collisional porphyries (e.g., Shafiei et al., 2009; Richards et al., 2012; Asadi et al., 2014; Zarasvandi et al., 2013, 2015a, 2018; Rezaei, 2017). This belt contains at least two giant deposits namely Sarcheshmeh (1200 Mt, 0.6% Cu, 0.02% Mo; Shafiei and Shahabpour, 2008), and Sungun (500 Mt, 0.7% Cu, 0.01% Mo; Hezarkhani and Williams-Jones 1998), and one large deposit (Meiduk: 170 Mt, 0.86% Cu, 0.007% Mo, 82 ppb Au, 1.8 ppm Ag; Taghipour et al., 2008), as well as several medium-sized to small low grade porphyry Cu  $\pm$  Mo systems (e.g., Sarkuh, Abdar, Iju, Keder, Dalli, Chahfiruzeh; Fig. 1a and b; Table 1).

During the recent years several studies have been carried out for characterizing the main factors controlling the metal fertility of porphyry copper systems (e.g., Audetat et al., 2008; Richards, 2013; Williamson, 2016; Wang et al., 2018; Zarasvandi et al., 2018). For example as mentioned in Richards (2013), optimum coincidence of some non-unique geological factors, i.e., distinct tectonic setting and focused fluid flow may explain the enhancement of mineralization degree in the world class giant porphyry Cu intrusions. Moreover, the detailed

\* Corresponding author.

E-mail address: [Zarasvandi\\_a@scu.ac.ir](mailto:Zarasvandi_a@scu.ac.ir) (A. Zarasvandi).

<https://doi.org/10.1016/j.oregeorev.2018.12.027>

Received 17 October 2018; Received in revised form 13 December 2018; Accepted 30 December 2018

Available online 31 December 2018

0169-1368/© 2018 Elsevier B.V. All rights reserved.

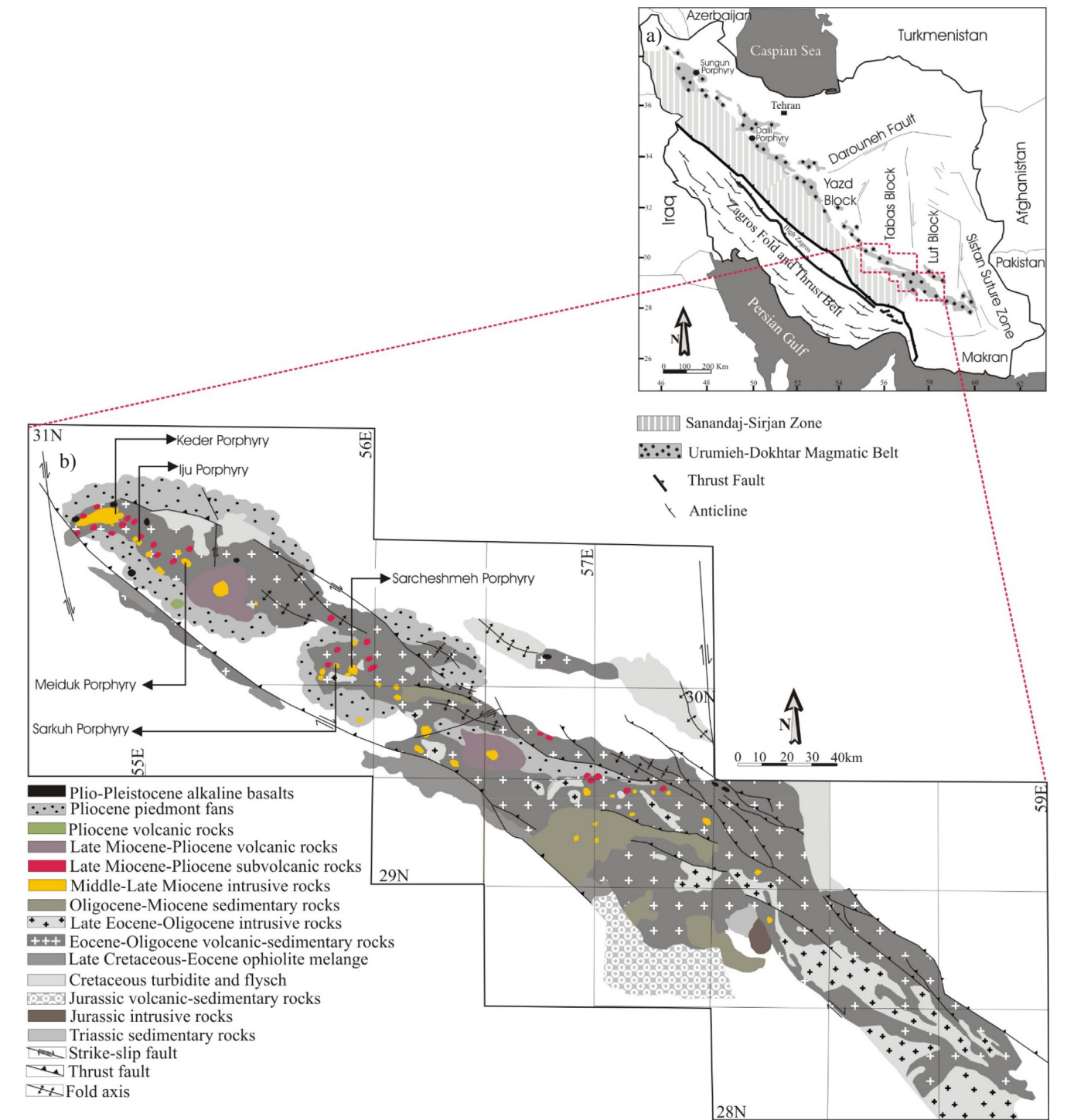


**Fig. 1.** (a) Zagros orogenic belt in western Iran with its three major NW-SE trending tectonic zones – Zagros Fold and Thrust Belt (ZFTB), Sanandaj-Sirjan Zone (SSZ), and Urumieh-Dokhtar Magmatic Belt (UDMB); (b) Geological map of SE part of UDMB and location of studied porphyry copper deposits; modified after [Shafiei et al. \(2009\)](#).

**Table 1**  
General features of selected porphyry deposits in UDMA ([Zarasvandi et al., 2018](#)).

Porphyrydeposit	Radiometric Age (Ma)	Dating method	Sample material	Porphyry Intrusion	Tonnage (Mt)	Grade
Meiduk	12.5 ± 0.5	U–Th/He	Single zircon	Granodiorite	170	0.86% Cu
Iju	9.27 ± 0.50	U–Th/Pb	Single zircon	Granodiorite, tonalite	74	0.31% Cu
Sarkuh	15.18 ± 0.43	U–Pb	Zircon	Granite, granodiorite	110	0.26% Cu
Keder	–	–	–	Quartz diorite, diorite	–	0.06–0.16% Cu

characterization of the magmatic history and petrogenetic evolution of porphyry-bearing magmatic belts have also proved that these features play an important role in the metal endowment of porphyry copper systems (Richards et al., 2012; Asadi et al., 2014; Wang et al., 2014; Zarasvandi et al., 2015a,b). Comparing the overall features of barren and mineralized porphyry intrusions, Wang et al. (2018) proposed that barren alkali-rich porphyries contain numerous primary melt inclusions, with no significant co-occurrence of fluid inclusions. In contrast mineralized Cu (Au, Mo) porphyries are characterized by notably rare occurrence of melt inclusions and contain mostly fluid inclusions having halite, sylvite, calcite daughter minerals (Wang et al., 2018). As emphasized by Richards (2016), the fact is that the most porphyry intrusions are not linked with considerable mineralization. Generally, they encompass a spectrum of low-grade to high-grade mineralization with only punctiform development of giant ore systems (Richards, 2016; Rezaei, 2017; Zarasvandi et al., 2018). Hence, an optimum coincidence of several mechanisms and processes must occur for enhancing the ore efficiency in porphyry systems (Richards, 2013, 2016). Whereas the generation and fluid evolution of subduction-related porphyries have been well documented, collisional ones are less well understood especially through factors controlling metal fertility. In the present paper we focus on the hydrothermal fluid evolution in some Miocene collisional porphyry copper systems in UDMB (Fig. 1b, Table 1). The fluid inclusion data provide an insight into the factors controlling the metal fertility of collisional porphyry copper systems.

## 2. Regional geological setting

The Tethyan orogen extends over 12,000 km from the Alps, across SE Europe, Turkey, Iran, Pakistan, Tibet, Indochina to southwest Pacific (Richards et al., 2012; Richards, 2015a,b). This belt is characterized by separate segments containing collided arcs but also there is oceanic lithosphere that is still being subducted (e.g., Makran zone in SE Iran; Richards, 2015b). The Zagros orogenic and metallogenic belt is one of these segments in western Tethyan realm. It consists of three main tectonic zones, namely the Zagros Fold and Thrust Belt (ZFTB), the Sanandaj-Sirjan Zone (SSZ) and the Urumieh-Dokhtar Magmatic Belt (UDMB; Fig. 1a).

The UDMB extends over about 2000 km from NW to SE of Iran. This is positioned between the SSZ and continental blocks of the Central Iran structural zone (Alavi, 2007; Fig. 1a). It is dominated by calc-alkaline and in some parts alkaline igneous rocks generated during subduction and closure of Neo-Tethys followed by continent–continent collision in Paleogene – Neogene times (e.g., Berberian et al., 1982; Mohajjel et al., 2003; Ricou, 1994). In the UDMB, Late Paleocene-Eocene volcanic rocks were generated during the extensional arc flare-up owing to the episodes of slab retreat or slab rollback (Verdel, 2011). Subsequently, Oligocene–Miocene intrusions were emplaced into the Eocene volcanic and volcanoclastic rocks. Considering porphyry emplacement, a trend of increase in arc maturation, crustal thickness, and consequently transition of magmatism from normal andesitic calc-alkaline to adakite-like high K calc-alkaline affinity has been identified in the UDMB. This is similar to what has been reported previously from Chagai volcano-plutonic belt in Pakistan and Gangdese belt in Tibet (Richards et al., 2012; Wang et al., 2014; Zarasvandi et al., 2015a, 2018). It should be noted that the large porphyry systems in the UDMB are strictly associated with Miocene adakite-like high Sr/Y intrusions that were emplaced about 30 m.y. after the onset of igneous activities, especially in the southeastern parts of UDMB (Zarasvandi et al., 2015b, 2018; Fig. 1b, Fig. 2). In contrast to classic subduction-related models, recent studies proposed that the fertile Miocene porphyries mostly formed by partial melting of thickened mafic lower crustal rocks where compression and tectonic shortening led to the development of a garnet–amphibolite melting zone in the lower crust during continent–continent collision (Shafiei et al., 2009; Asadi et al., 2014; Zarasvandi et al., 2015a, 2018).

## 2.1. Local geology

### 2.1.1. Sarkuh

The Sarkuh porphyry Cu  $\pm$  Mo deposit (110 Mt sulphide ore, and 0.26% Cu, Table 1) is located 6 km NW of Sarcheshmeh mine (Aghazadeh et al., 2015; Fig. 1b). An E-W elongated stock composed of a granodiorite core and a granite rim is emplaced within Eocene basaltic andesite, andesite, pyroclastic breccias, and tuffs (Nourali and Mirnejad, 2012). The intrusion has been dated at  $15.18 \pm 0.43$  Ma (U-Pb zircon dating, McInnes et al., 2005). Late stage microcrystalline quartz diorite porphyry dikes crosscut the Sarkuh stock especially in the central parts of the deposit. Hydrothermal alteration consists of potassic, potassic-phyllitic, phyllic, argillic and propylitic alterations (Nourali, 2011). In the Sarkuh porphyry, early potassic and propylitic alterations are followed by later argillic and phyllic alterations. Intermediate alterations i.e., potassic – argillic, potassic – phyllic, as well as rare silicic alterations were also observed. Copper contents gradually decrease from the potassic zone in the central parts to the transitional potassic-phyllitic and phyllic zones (Nourali and Mirnejad, 2012). The potassic alteration is widely distributed with biotite being the dominant minerals; magmatic biotite was re-equilibrated and new hydrothermal biotite formed. Hornblende and biotite are partly to completely replaced by chlorite. Also, early stage hydrothermal biotite veinlets indicative of beginning potassic alteration crosscut plagioclase and magmatic biotite (i.e., Sillitoe, 2010; Fig. 3a). Monazite is a rare accessory phase in the potassic alteration zone at Sarkuh deposit (Fig. 3b). On the contrary, phyllic alteration consist mainly of quartz, clay, sericite, pyrite, and chlorite has limited extent in the Sarkuh porphyry system. The large-scale propylitic alteration zone seems to be restricted to the shallow levels of the deposit (Mirnejad et al., 2013). Based on crosscutting relations and vein mineralogy five major types of veinlets can be distinguished which form three main mineralization stages in the Sarkuh deposit: (1) Pre-ore stage veinlets associated with potassic alteration; assemblages include quartz + K-feldspar and quartz + biotite (Fig. 4a), (2) Main ore stage including veins with quartz + biotite + chlorite  $\pm$  magnetite  $\pm$  pyrite  $\pm$  chalcopryrite in the potassic alteration zone, and younger quartz veinlets with pyrite + chalcopryrite  $\pm$  bornite  $\pm$  chalcocite  $\pm$  sericite in the potassic – phyllic transition zone (Fig. 4b), and (3) Late stage barren quartz  $\pm$  calcite veinlets associated with phyllic alteration (Fig. 4c).

### 2.1.2. Meiduk

The granodiorite stock of Meiduk Cu  $\pm$  Mo deposit ( $12.5 \pm 0.1$  Ma, McInnes et al., 2005) is located in the northwestern part of the Kerman Cenozoic magmatic arc, 70 km NW of the giant Sarcheshmeh porphyry copper deposit (Fig. 1b). The deposit contains 170 Mt supergene and hypogene ores with a grade of 0.86% Cu, 0.007% Mo and 82 ppb Au (Table 1; Taghipour et al., 2008). It is hosted in the Mid-Late Eocene Razak complex ( $37.5 \pm 1.4$  Ma,  $^{40}\text{Ar}/^{39}\text{Ar}$  age of albite), which is dominated by basaltic to rhyolitic volcanoclastic sequences (Hassanzadeh, 1993; Fig. 2a). In the Meiduk deposit, the granodiorite stock is cross-cut by a swarm of NNE-trending dykes and exhibits strong potassic alteration. This is characterized by disseminated K-feldspar, chlorite, and magnetite (Fig. 3c), with relicts of hornblende and plagioclase. The latter is partly to completely replaced by hydrothermal biotite (Fig. 3d). Also, the replacement of biotite and hornblende with chlorite were seen in the potassic alteration. Potassic to phyllic transition containing biotite, sericite, K-feldspar as well as rare occurrence of tourmaline and chlorite were identified in the Meiduk porphyry system. Strong sericitization lead to the widespread transformation of feldspar and biotite to sericite in the phyllic alteration. This is also dominated by disseminated pyrite and quartz-sericite veins and veinlets. Typically, three distinct zones of Cu mineralization can be distinguished in the Meiduk deposit, namely hypogene ore zone, the supergene enrichment zone, and the leached zone cap (“leached cap”, Rezaei, 2017). Based on mineralogy and cross-cutting relations of



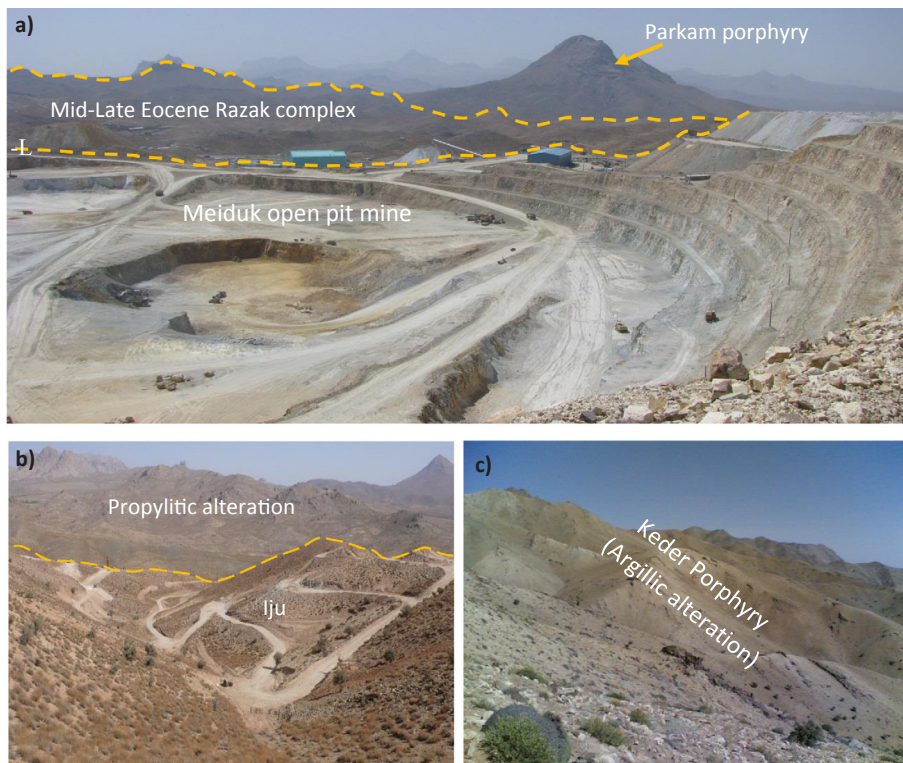


**Fig. 2.** Field photographs (a) Meiduk mine with Parkam porphyry stock in the background (view to south) intruding the volcanic rocks of Mid-Late Eocene Razak Complex ; (b) Iju porphyry with phyllic alteration zone (light-brown) in the foreground and propylitic alteration zone (dark brown) in the background (view to north); (c) Argillic alteration in the Keder porphyry deposit (view to west).

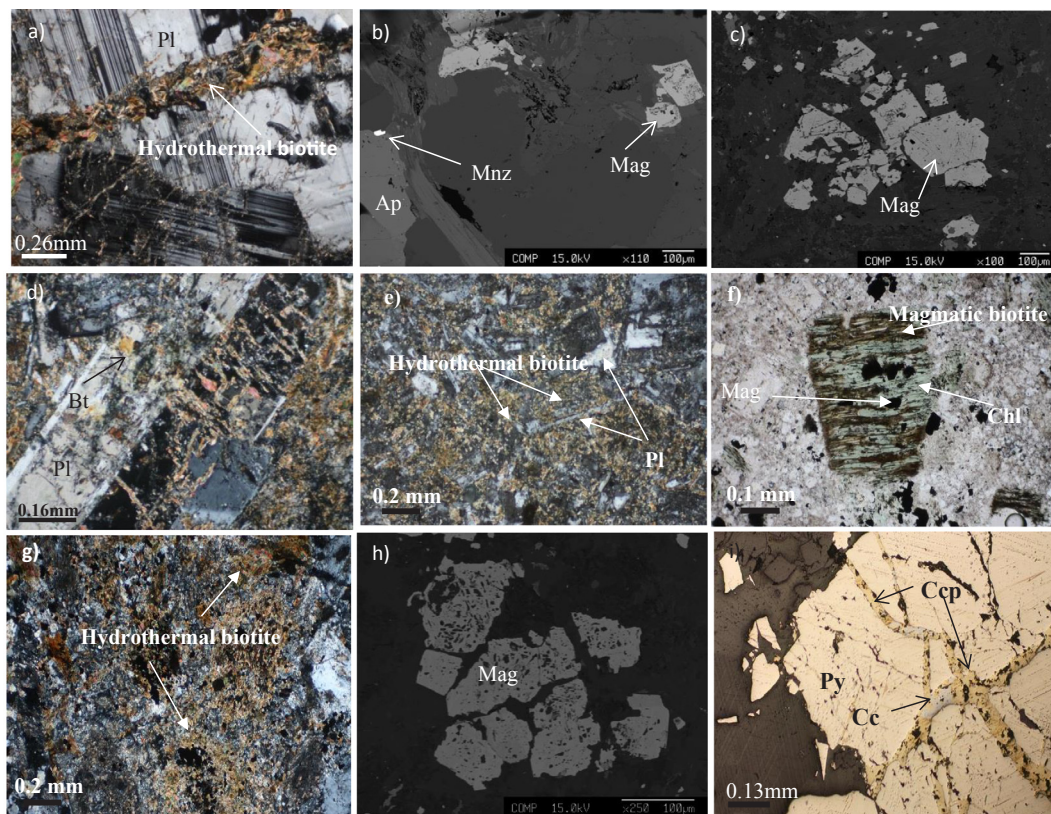


**Fig. 3.** Photomicrographs and SEM backscattered electron (BSE) images (a) Early hydrothermal biotite veinlet crosscutting plagioclase, potassic alteration, Sarkuh deposit, transmitted light, crossed polarizers; (b) Fine-grained magnetite (Mag) associated with apatite (Ap) and monazite (Mnz), Sarkuh deposit, BSE; (c) Disseminated magnetite (Mag), Meiduk deposit, BSE; (d) Plagioclase (Pl) partly replaced by hydrothermal biotite (Bt), potassic alteration, Meiduk deposit, transmitted light, crossed polarizers; (e) Disseminated hydrothermal biotite partly replacing plagioclase (Pl), Iju deposit, transmitted light, crossed polarizers; (f) Chlorite + magnetite replacing magmatic biotite, Iju deposit, transmitted light, parallel polarizers; (g) Strong pervasive biotitization in the potassic alteration zone, Keder deposit, transmitted light, crossed polarizers; (h) Fine-grained magnetite (Mag), Iju deposit, BSE; (i) Chalcopyrite partly replaced by chalcocite filling microfractures within pyrite, Keder deposit, reflected light.



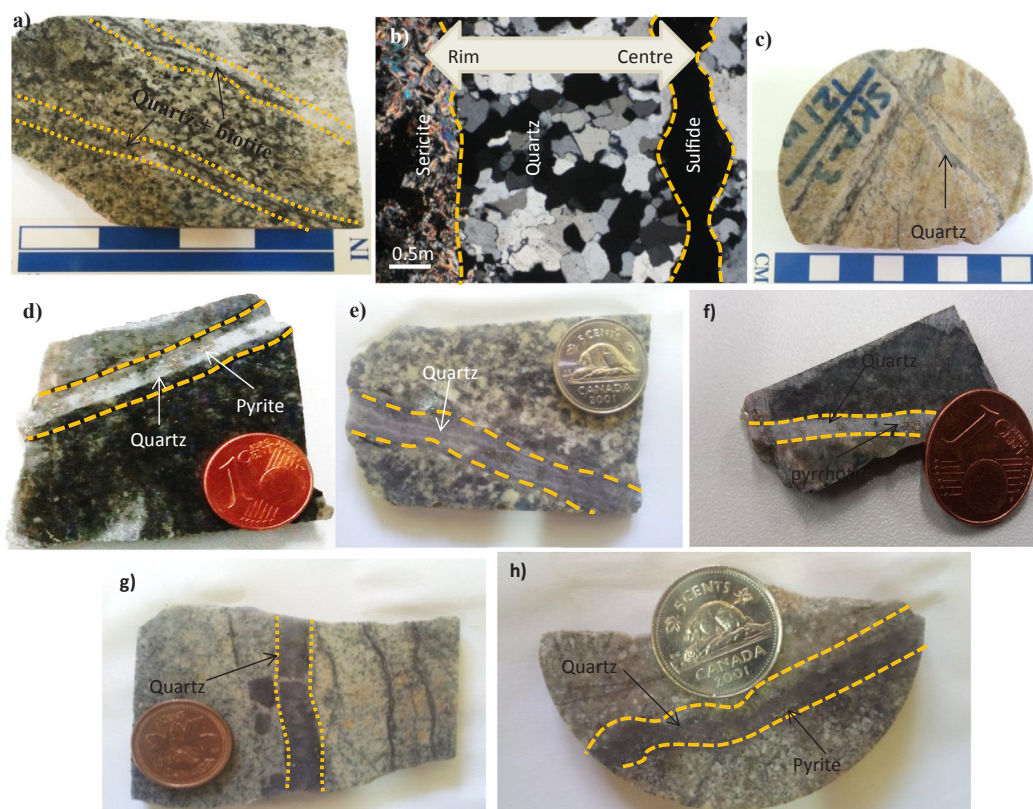


**Fig. 4.** (a) Pre-ore stage veinlets with quartz + biotite, potassic alteration zone, Sarkuh deposit; (b) Quartz-sulfide veinlet with sericite alteration at rim, main mineralization stage, Sarkuh deposit; (c) Late-stage barren quartz veinlet, Sarkuh deposit; (d) Early pre-ore stage quartz veinlet with some pyrite, potassic alteration zone, Meiduk deposit; (e) Late stage veinlet with quartz  $\pm$  pyrite  $\pm$  sericite, Meiduk deposit; (f) Early hydrothermal quartz veinlet with pyrrhotite, potassic alteration zone, Iju deposit; (g) Late stage barren quartz veinlets, Iju deposit; (h) Late stage quartz-pyrite vein, Keder deposit.

veins/veinlets, three main mineralization stages are identified in the Meiduk deposit. (1) Early stage veinlets with the assemblage of quartz  $\pm$  K feldspar  $\pm$  pyrite  $\pm$  magnetite associated with potassic alteration (Fig. 4d). (2) Main ore stage developed mostly in the potassic alteration and potassic-phyllic alteration zones. This stage is characterized by veinlets containing quartz + pyrite + chalcopyrite  $\pm$  chalcocite  $\pm$  bornite with some veinlets showing a sericite alteration halo. (3) Late stage veinlets with quartz  $\pm$  pyrite  $\pm$  sericite which predominantly occur in the phyllic alteration zone (Fig. 4e).

### 2.1.3. Iju

The Iju porphyry Cu  $\pm$  Mo deposit is located 72 km NE of Shahr-e-Babak city in the Kerman segment of UDMB (Fig. 1b and 2b). Based on the available U-Pb zircon dates, porphyry emplacement is dated at  $9.27 \pm 0.50$  Ma and coeval with other collisional porphyries in the UDMB (McInnes et al., 2005). The Eocene volcanic and pyroclastic sequences exposed at Iju are composed of andesitic breccia, tuffaceous breccia, tuff, and agglomerate with some minor intercalations of lava flows of basaltic andesite and andesite. The main porphyry stock is crosscut by dioritic to quartz-dioritic dykes. Based on field observations and petrographic studies a main tonalite intrusion is recognized as well as smaller intrusions ranging in composition from quartz diorite and granodiorite to granite. The rocks hosting Cu-mineralization have undergone variable degrees of hydrothermal alteration, namely potassic, potassic-phyllic, phyllic, propylitic, and argillic. The potassic alteration zone at Iju is of limited extent, but contains most of the Cu mineralization. Spatially, potassic alteration is intimately associated with phyllic alteration, with some parts being overprinted by phyllic alteration. The potassic alteration is characterized by ubiquitous

occurrence of fine grained disseminated hydrothermal biotite in the groundmass. This is also formed by replacement of hornblende and plagioclase (Fig. 3e). Fine-grained magnetite is generally accompanied with biotite chloritization (Fig. 3f). The phyllic alteration containing quartz + sericite + pyrite  $\pm$  carbonate is mainly accompanied with granodiorite intrusions in the central parts of deposit (Golestani et al., 2018).

At Iju, propylitic alteration with dominant phases of calcite and chlorite mainly occurs in the western and south western parts of the deposit; it is especially developed in the volcanic host rocks (Mirnejad et al., 2013). Argillic alteration is of limited extent (Mirnejad et al., 2013). Three mineralization stages are distinguished at Iju: (1) Pre-ore stage veinlets containing quartz  $\pm$  pyrrhotite  $\pm$  magnetite  $\pm$  K feldspar, which are associated with potassic alteration and lack sericite selvages (Fig. 4f), (2) Main mineralization stage veinlets are hosted in the potassic with less commonly in the phyllic alteration. They contain quartz + chalcopyrite + pyrite  $\pm$  molybdenite  $\pm$  sericite. (3) Late stage barren quartz  $\pm$  calcite  $\pm$  sericite veinlets, which crosscut the earlier ones (Fig. 4g).

### 2.1.4. Keder

The Keder porphyry Cu deposit is located in the NE part of Kerman segment of UDMB (Fig. 1b). There, intrusive rocks include diorite to quartz diorite containing plagioclase and quartz, with minor hornblende, biotite, and K-feldspar (< 5 vol%). The plutonic rocks intruded into northeast-dipping Eocene volcanic sequences, which are predominantly low-K calc-alkaline plagioclase-phyric andesites. In the Keder area, argillic alteration is volumetrically most abundant (Fig. 2c). However, there are subordinate occurrence of propylitic and phyllic

alterations (Ghorbani and Ebrahimi, 2009). The latter contain quartz + pyrite + sericite  $\pm$  carbonate  $\pm$  rutile. Limited occurrence of potassic alteration was identified only in the deepest parts of the deposit in drill holes. This is characterized by disseminated hydrothermal biotites and newly formed re-equilibrated magmatic biotite (Fig. 3g) with some parts magnetite and pyrite occurring as veinlets or disseminations (Fig. 3h). The rare occurrence of chalcopyrite is mostly fills the micro-fractures of pyrite (Fig. 3i). The argillic alteration is recognized by bleaching of feldspars and it extends toward the pyrite shell, which consists of pyrite and minor chalcopyrite and specular hematite that commonly replaces magnetite. The feldspar has albite composition in the proximal part of the argillic alteration zone, whereas in the distal zone varies from andesine to oligoclase, especially around the pyrite shell (Taghinejad, 2012). Mineralogy and crosscutting relations have revealed that the early mineralization stage in the Keder porphyry is represented by veinlets with quartz  $\pm$  K-feldspar  $\pm$  magnetite  $\pm$  pyrite. This is followed by later quartz  $\pm$  pyrite  $\pm$  chalcopyrite veinlets in the potassic-phylic alteration zone. The main mineralization stage includes quartz veinlets with pyrite  $\pm$  chalcopyrite, and these are crosscut by late stage, pyrite-bearing quartz veins (Fig. 4h).

### 3. Material and methods

All samples were selected from drill cores with emphasis on vein types and their enclosing alterations, especially those from potassic and phyllic alteration assemblages. Based on crosscutting relationships and the presence of well-developed mineralogical/textural features, more than 50 samples from the four studied deposits were selected for the preparation of doubly polished thick wafers ( $\sim 0.2$ – $0.3$  mm) at Montanuniversität Leoben, Austria.

All fluid inclusion measurements were done at the Fluid Inclusion Laboratory of Montanuniversität Leoben. Microthermometric measurements were performed with a Linkam THMSG 600 freezing-heating stage equipped with an Olympus microscope (Table 2). The stage was calibrated at temperatures of  $+374.1$  °C,  $0.0$  °C, and  $-56.6$  °C using synthetic  $\text{H}_2\text{O}$ – $\text{CO}_2$  fluid inclusions prepared in the same laboratory. For microthermometric measurements, the upper and lower temperature thresholds were  $600$  °C and  $-120$  °C, respectively. The heating rate was generally  $1$  °C/min, when temperatures of homogenization or ice melting were determined.

Laser Raman micro-spectroscopy was carried out in order to correctly characterize the liquid, vapour, and solid phases of the studied fluid inclusions. The data were obtained using a Jobin Yvon LabRAM Raman spectrometer. The LabRAM is operated with an Olympus microscope, and a LPlanFI 100x/0.80 numerical aperture objective lens. A frequency doubled 100 mW Nd-YAG laser with an excitation wavelength of  $\lambda = 532.068$  nm is used, with a laser power of about  $1$ – $2$  mW at the sample surface. The scattered light is dispersed by a 1800 grooves/mm gratings. The detector is an air cooled (Peltier) CCD-3000 ( $1024 \times 256$  pixels) operating at  $-60$  °C. Spectra are collected using multiple spectral windows between  $100$  and  $3000$   $\text{cm}^{-1}$ , corresponding to a pixel resolution of about  $1.64$   $\text{cm}^{-1}$  at relative low wavenumbers, and  $1.35$   $\text{cm}^{-1}$  at relative high wavenumbers. A  $100$   $\mu\text{m}$  slit width combined with a  $1000$   $\mu\text{m}$  confocal hole aperture is used to obtain the best resolved spectra. Neon emission lines and Raman spectra of silicon ( $520$   $\text{cm}^{-1}$ ), polyethylene ( $1062$   $\text{cm}^{-1}$ ,  $1128$   $\text{cm}^{-1}$ ,  $1169$   $\text{cm}^{-1}$ ,  $1295$   $\text{cm}^{-1}$ ,  $1487$   $\text{cm}^{-1}$ ,  $1439$   $\text{cm}^{-1}$ ,  $2848$   $\text{cm}^{-1}$ ,  $2881$   $\text{cm}^{-1}$ ), are used for calibration. Also, in some cases, artificial background effects of Raman spectra were removed using CrystalSleuth software.

## 4. Results

### 4.1. Fluid inclusion petrography

In the studied porphyry copper systems, textural criteria described

by Roedder (1979) have been used for the discrimination of primary, secondary, and pseudosecondary inclusions in the different stages of mineralization. Detailed FI petrography and classification of fluid inclusions for the all mineralization stages are presented below.

#### 4.1.1. Sarkuh porphyry

Based on the composition and phases present at room temperature, three main types of fluid inclusions were identified in the hydrothermal veins of Sarkuh porphyry copper system (Fig. 5). They include (1) liquid-rich two phase aqueous (liquid  $\text{H}_2\text{O}$  + vapor  $\text{H}_2\text{O}$ , LV; Fig. 5a), (2) vapor-rich two phase aqueous-carbonic (vapor  $\text{H}_2\text{O}/\text{CO}_2$  + liquid  $\text{H}_2\text{O}$ , VL; Fig. 5b), and (3) solid- or daughter mineral-bearing multiphase inclusions (S-type; Fig. 5c and d). Considering presence or absence of halite, the S-type inclusions could be subdivided into two subtypes: (1) SH subtype inclusions containing halite cube, as well as other solid phases such as hematite, chalcopyrite, siderite, and pyrite (Fig. 5c), and (2) SM inclusions containing mostly magnetite and/or pyrite as solid phase, but without a halite crystal (Fig. 5d).

The VL inclusions are most abundant in quartz veinlets of the pre-ore and the main mineralization stages. They are negative, rounded or irregular in shape with size ranging from  $3$  to  $23$   $\mu\text{m}$ . As confirmed by laser Raman spectroscopy, a few VL inclusions in pre-ore stage, main ore, and late stage contain  $\text{CO}_2$  vapor components. In contrast, aqueous LV inclusions are present mostly in late-stage barren quartz veinlets. They are usually of irregular or rounded shape, with a diameter ranging between  $3$  and  $16$   $\mu\text{m}$ , rarely up to  $25$   $\mu\text{m}$ . The S-type inclusions are present in the pre-ore stage and main ore stage quartz veinlets. The SM inclusions are more frequent in the pre-ore stage, while SH inclusions mostly are assigned to the main ore stage. Both SM and SH inclusions are rounded or of negative shape, with diameters ranging between  $5$  and  $23$   $\mu\text{m}$  and  $6$ – $17$   $\mu\text{m}$ , respectively.

#### 4.1.2. Meiduk porphyry

Three main types of fluid inclusions were also recognized in the hydrothermal veins in the Meiduk porphyry copper system. They include liquid-rich two phase (liquid  $\text{H}_2\text{O}$  + vapor  $\text{H}_2\text{O}$ , LV), vapor-rich two phase (vapor  $\text{H}_2\text{O}/\text{CO}_2$  + liquid  $\text{H}_2\text{O}$ , VL), and solid- or daughter mineral-bearing multiphase inclusions (S-type; Fig. 6). In the Meiduk hydrothermal system, the VL inclusions are well developed in the early and main ore stages (Fig. 6a), while S-type inclusions are present from early to late stages of mineralization (Fig. 6b). In the early pre-ore stage, most of VL inclusions contain  $\text{CO}_2$  vapor component with the vapor phase being volumetrically dominant, and generally occur in negative, irregular or rounded shapes (Fig. 6c). These inclusions range in diameter from  $7$  to  $25$   $\mu\text{m}$ . In contrast, LV inclusions are smaller in size ( $3$  to  $12$   $\mu\text{m}$ ), and usually are shapeless or may have rounded or negative shapes (Fig. 6d). As confirmed by laser Raman spectroscopy, some of the S-type inclusions especially in the early stage quartz veins contain  $\text{CO}_2$  vapor constitutes (Fig. 6a). These multiphase inclusions contain liquid ( $\text{H}_2\text{O}$ ) + vapor ( $\text{H}_2\text{O}/\text{CO}_2$ ) and the solid phases halite + hematite  $\pm$  anhydrite  $\pm$  magnetite  $\pm$  chalcopyrite  $\pm$  pyrite  $\pm$  siderite (Fig. 6a). Among the solid phases, hematite and anhydrite are most abundant in S-type inclusions of the early stages of mineralization. S-type inclusions generally have irregular or rounded shapes with diameters ranging mostly between  $5$  and  $15$   $\mu\text{m}$  and rarely up to  $23$   $\mu\text{m}$ . It is important to note that, in the ore stage, S-type inclusions with a relatively large vapor bubbles coexist with VL inclusions.

#### 4.1.3. Keder porphyry

Considering the small size ( $< 5$   $\mu\text{m}$ ) of fluid inclusions in early stage veinlets, we focused on the quartz veinlets hosting in pyrite (main stage), and pyrite-bearing quartz veins (late stage) to investigate the fluid evolution of the Keder porphyry copper system. In this deposit, also three main groups of fluid inclusions have been recognized: (1) Liquid-rich two phase (liquid  $\text{H}_2\text{O}$  + vapor  $\text{H}_2\text{O}$ , LV; Fig. 7a), (2)

**Table 2**  
Microthermometry data of fluid inclusions in the studied porphyry copper systems.

Porphyry/Mineralization stage	Inclusion type	Number	T <sub>h</sub> (°C)	T <sub>m (Ice)</sub> (°C)	Te (°C)	T <sub>m (Halite)</sub> (°C)	T <sub>mCO2</sub> (°C)	T <sub>mCLAT</sub> (°C)	Salinity (wt.% NaCl)			
Sarkuh	SM	13	490–585	–4.2- –16.2	–21.6- –55.1	238.9–342.3		1.9–3.4	6.6–19.5			
	SH	7	421.6–572.3						34–41.67			
	VL	11	420–578	–5.4- –16.2	–21.2- –54.1				8.3–19.58			
	C	5	401.1–542.3						11.33–13.3			
	Early stage	SM	10	358.2–477.2	–2.2- –12.6	–31.2- –63.6	167.2–334.5			3.59–16.5		
		SH	21	345.4–469.6						30.3–41		
		VL	15	362.4–434.9	–1.1- –9.7	–21.4				1.8–13.6		
		LV	3	356.9–411	–8.8- –12.3					12.6–16.2		
		C	4	362.3–377.1						–56.6- –57.2	4.2–5.9	7.5–10.1
	Ore stage	SM	2	158.2–276.6	–0.6- –3.2		192.2–244			0.99–5.1		
SH		9	160.8–377.7			31.4–34.3						
LV		16	154.1–315.2	–0.5- –10.6	–19- –28	0.82–14.5						
C		1	337.4			–58.2				8.9	2.1	
Porphyry/Mineralization stage	Inclusion type	Number	T <sub>h</sub> (°C)	T <sub>m (Ice)</sub> (°C)	Te (°C)	T <sub>m (Halite)</sub> (°C)	T <sub>mCO2</sub> (°C)	T <sub>mCLAT</sub> (°C)	Salinity(wt.% NaCl)			
Meiduk	SH	35	399–598			276.8–570.3		1.1–2.4	36.4–73.2			
	VL	10	429.6–579.2	–14.3- –19.2	–29.8				16.9–21.8			
	C	10	416.1–586.5						–56.6- –59.8	12.6–14.3		
	SH	22	312–480						286.4–414	37.1–48.9		
	Ore stage	LV	6	239.8–348.4	–5.3- –18.6	–40				8.2–21.3		
		VL	8	335.1–386.1	–5.2- –15.4					8.09–18.9		
		SH	5	247–371						237–371.2	33.8–44.4	
	Late stage	LV	6	272.6–357.3	–0.9- –12.3	–20.1				1.4–16.2		
	Porphyry/Mineralization stage	Inclusion type	Number	T <sub>h</sub> (°C)	T <sub>m (Ice)</sub> (°C)	Te (°C)	T <sub>m (Halite)</sub> (°C)		T <sub>mCO2</sub> (°C)	T <sub>mCLAT</sub> (°C)	Salinity(wt.% NaCl)	
Iju	SH	36	503.1–590			348.1–580.1			42.2–71.07			
	VL	9	500–575.1	–9.6- –20.1					13.5–22.4			
	SH	13	391–509						328.9–509.1	40.4–60.9		
	VL	7	390.1–480	–6.4- –20.1					9.7–22.4			
	Ore stage	LV	1	495.1	–4.1				6.52			
		SH	7	263–410					230–410		33.4–48.5	
		LV	9	219.3–386.1	–0.1- –7.1						0.16–10.6	
	Late stage	VL	8	326–394.1	–1.7- –12.5						2.7–16.4	
	Porphyry/Mineralization stage	Inclusion type	Number	T <sub>h</sub> (°C)	T <sub>m (Ice)</sub> (°C)	Te (°C)	T <sub>m (Halite)</sub> (°C)		T <sub>mCO2</sub> (°C)	T <sub>mCLAT</sub> (°C)	Salinity(wt.% NaCl)	
Keder	SH	14	438–535			302–500			38.3–59.7			
	SM	3	510–546	–15.1- –21.3					18.7–23.1			
	VL	9	450–570	–1.3- –19.3					2.1–21.8			
	SH	37	246–415.1						28.4–49.1			
	Late stage	LV	16	190.6–387.3	–0.5 - –5.1	–26.3- –51.4				0.82–7.9		
		VL	15	280.1–418.5	–1.9- –19.1					3.1–21.7		
		C	2	280.1–418.5						–56.6- –57.1	8.6–9.5	1.02–2.7

Vapor-rich two phase (vapor  $H_2O/CO_2$  + liquid  $H_2O$ , VL; Fig. 7b, d), and (3) Solid- or daughter mineral-bearing multiphase inclusions (S-type; Fig. 7c). Compared with Meiduk and Sarkuh, VL inclusions are less common in the Keder deposit, especially in the main ore stage (Fig. 7b). Also, as confirmed by laser Raman analysis, VL inclusions with  $CO_2$  vapor components are rare in the late stages of mineralization. The VL inclusions are elliptic or rounded isometric in shape with diameters ranging from < 5–15  $\mu m$ . In contrast with VL fluid inclusions, S-type inclusions are common in the main and late stages. They contain a halite crystal, as well as pyrite or magnetite with rare occurrences of chalcopyrite (Fig. 7c). S-type fluid inclusions are rounded, irregular or elliptic, ranging in diameter from 5 to 13  $\mu m$ . Coexisting of S-type and VL inclusions has not been commonly observed and the most of the VL inclusions occur in clusters, especially in the outer zones of quartz crystals of late stage veinlets (Fig. 7d). In the Keder deposit, the LV inclusions are also limited to the late stages quartz veinlets where they appear in clusters or isolated bubbles (Fig. 7a). They are rounded to negative in shape and range in diameter from < 3 to 15  $\mu m$ . It is important to note that, beside of primary fluid inclusions, re-

equilibrated inclusions were also observed in the Keder porphyry (Fig. 7e). Also, linear trails of secondary FI containing S-type inclusions are present in the main and late stages veinlets (Fig. 7a and f).

#### 4.1.4. Iju porphyry

At Iju there are also three main types of fluid inclusions: (1) Liquid-rich two phase (liquid  $H_2O$  + vapor  $H_2O$ , LV), (2) Vapor-rich two phase (vapor  $H_2O$  + liquid  $H_2O$ , VL), and (3) Solid- or daughter mineral-bearing multiphase inclusions (S-type; Fig. 8). The S-type inclusions contain liquid  $H_2O$ , vapor  $H_2O$ , and solid- or daughter minerals including magnetite and (or) hematite with minor anhydrite and pyrite (Fig. 8a and b). It is important to note that in this porphyry copper system the  $CO_2$  vapor constitutes has rarely been detected by laser Raman analysis. The S-type fluid inclusions are abundant in the early pre-ore and main ore stages. These inclusions are rounded isometric or of negative crystal shape with diameters ranging between 3 and 13  $\mu m$ . In the pre-ore and main ore stages, these inclusions are often randomly distributed (Fig. 8a) or occur as clusters, especially in the marginal zones of quartz crystals (Fig. 8b). Compared with S-type fluid



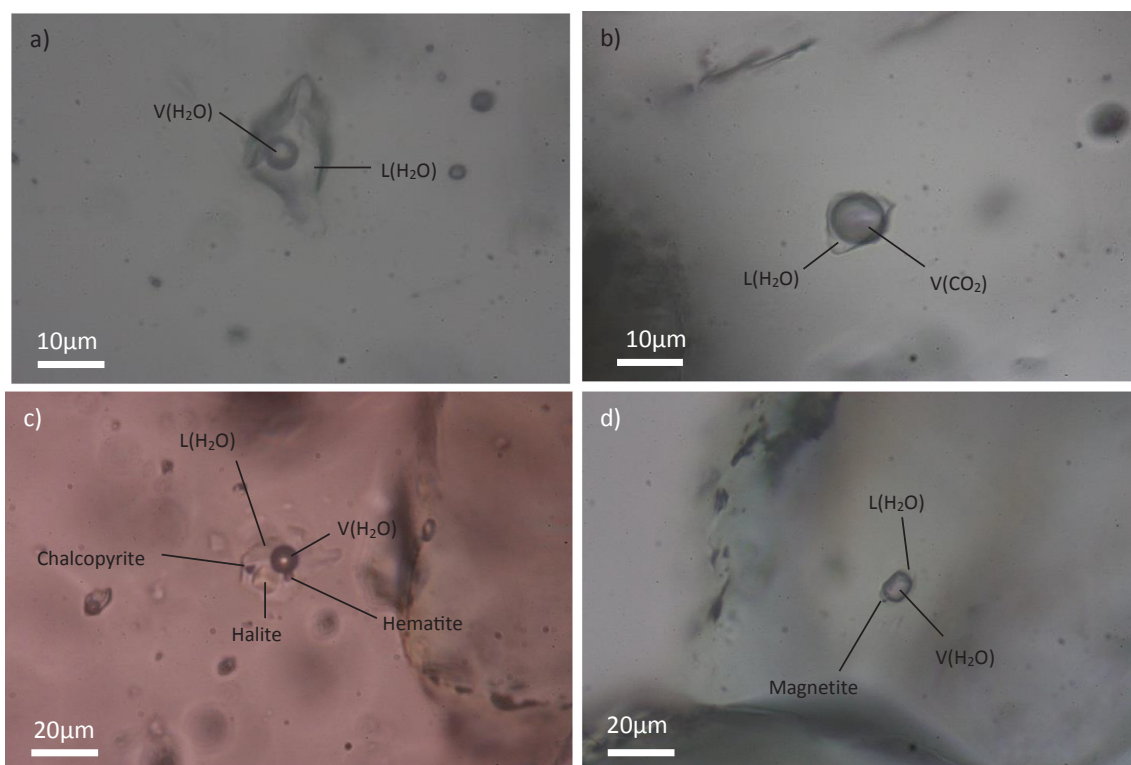


**Fig. 5.** Representative fluid inclusions in the Sarkuh porphyry copper deposit (a) Liquid-rich two phase aqueous inclusion (liquid H<sub>2</sub>O + vapor H<sub>2</sub>O) hosted in the late-stage barren quartz veinlets; (b) Vapor-rich two phase aqueous-carbonic (vapor CO<sub>2</sub> + liquid H<sub>2</sub>O) inclusion trapped in the pre-ore stage; (c) SH subtype inclusions containing halite, hematite and chalcopyrite solid phases; (d) SM inclusion containing magnetite in the veinlet of pre-ore stage.

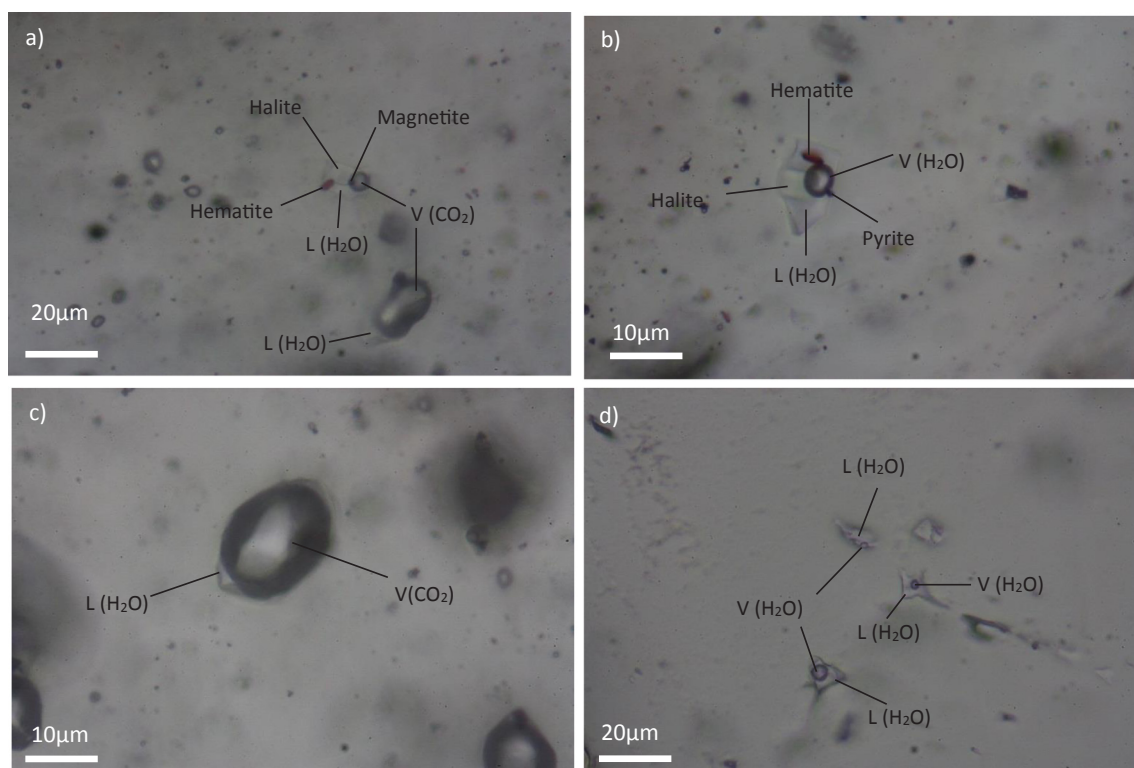


**Fig. 6.** Photomicrographs of various fluid inclusions in the Meiduk porphyry copper deposit (a) Coexistence of VL (vapor CO<sub>2</sub> + liquid H<sub>2</sub>O) and S-type inclusions in the early stage of mineralization; (b) Multiphase inclusions containing halite, pyrite and hematite solid phases in the main ore stage; (c) VL inclusion with CO<sub>2</sub> vapor component in the pre-ore stage; (d) Cluster of LV inclusions in the late stage veinlet.



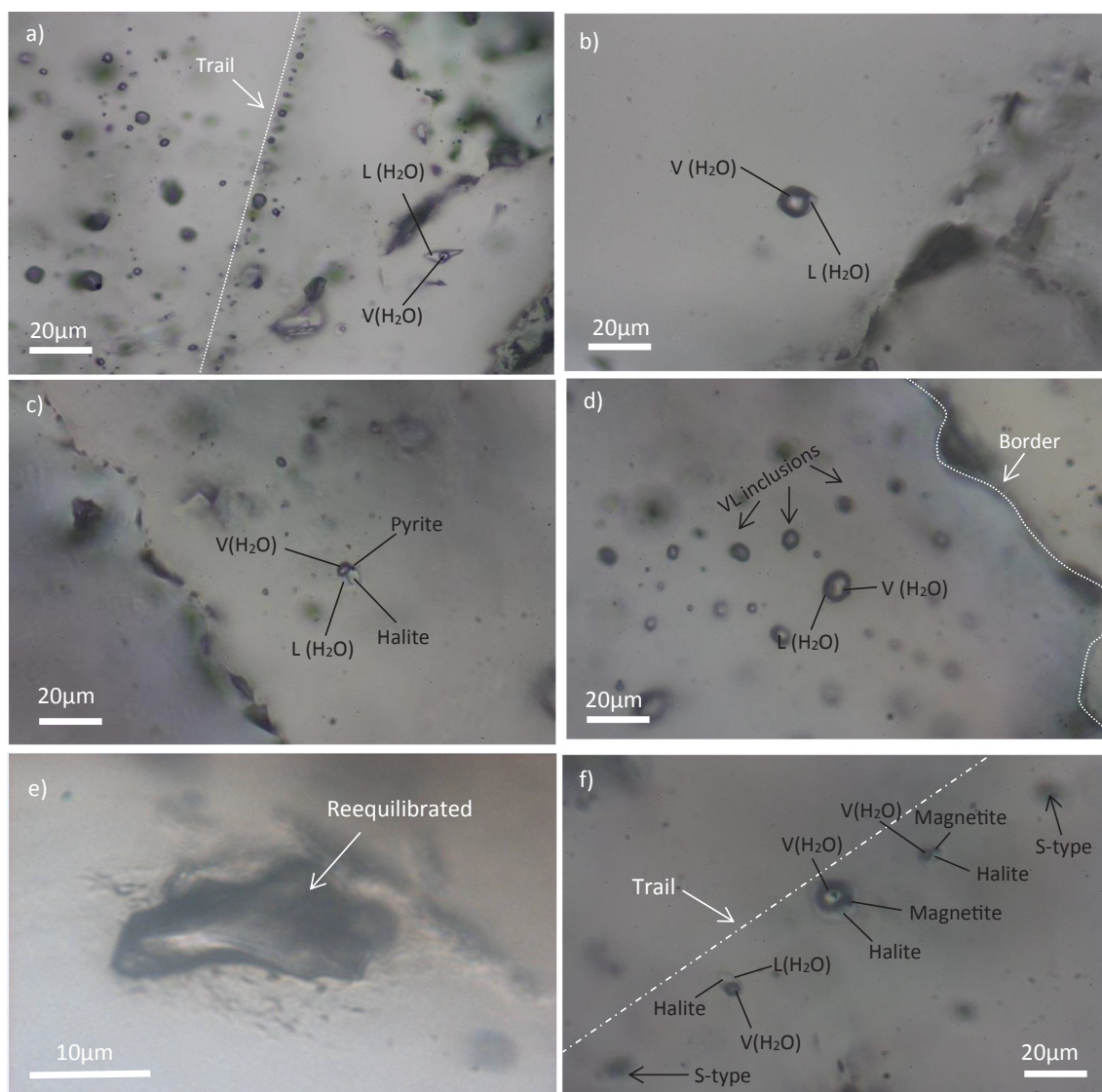


**Fig. 7.** Photomicrographs of representative fluid inclusions in the Keder porphyry copper deposit (a) LV inclusion in the late stage; (b) Isolate VL inclusion in the main ore stage; (c) Multiphase inclusion containing halite and pyrite in the main ore stage; (d) Cluster of VL inclusions in the border of quartz at the late of mineralization stage; (e) Re-equilibrated fluid inclusion in the main ore stage; (f) Linear inclusion trail in the main ore stage.

inclusions, the VL inclusions are present in all stages of mineralization. These inclusions are irregular or rounded with longest dimensions ranging from  $< 3 \mu\text{m}$  to  $15 \mu\text{m}$ . They can either be seen as individual inclusions or in trails. The latter are present mostly in late stage quartz veinlets (Fig. 8c). The LV fluid inclusions are generally  $< 3\text{--}20 \mu\text{m}$  in diameter and have elliptic or rounded shapes. In the ore-stage, LV inclusions can be found, but most of them occur in clusters or trails assemblages in late stage veinlets (Fig. 8d).

#### 4.2. Laser Raman spectroscopy analysis

Liquid, vapour, and solid phases of individual fluid inclusions were systematically analysed using laser Raman microspectroscopy (Figs. 9–11). Raman reference spectra in CrystalSleuth software and the main Raman bands ( $\text{cm}^{-1}$ ) listed in Frezzotti et al. (2012) have been used to confirm the identities of the analysed phases. The liquid phases of all inclusions from the different stages is dominated by  $\text{H}_2\text{O}$  as indicated by the broad Raman bands (Fig. 9). Importantly, with the exception of some LV inclusions, especially those trapped in the late stage veinlets (Fig. 9d–f), the Raman spectra of the liquid phase shows broadly overlapping bands in the OH stretching region

( $2750\text{--}3900 \text{ cm}^{-1}$ ; Fig. 9a–c), which conforms to interaction of Cl anions with water molecules in higher saline aqueous solutions (Sun, 2009; Frezzotti et al., 2012). Nevertheless, low chlorine contents ( $< 1 \text{ NaCl wt. \%}$ ) lead to the presence of two bands in the OH stretching region from  $2750$  to  $3900 \text{ cm}^{-1}$  as generally observed in liquid  $\text{H}_2\text{O}$  Raman spectrums (Fig. 9d–f; Frezzotti et al., 2012).

The vapour phase of almost all fluid inclusions also contains  $\text{H}_2\text{O}$  (e.g., Meiduk; Fig. 10a), although weak  $\text{CO}_2$  bands ( $1283$  and  $1387 \text{ cm}^{-1}$ ; Fig. 10b–d) were also detected.  $\text{CO}_2$  is present especially in some primitive multiphase inclusions (i.e., Meiduk porphyry), some VL inclusions of early stage veinlets and to a lesser extent in the veins of main mineralization stage (Fig. 10c) and late mineralization stages (Fig. 10d). The following solid phases as daughter minerals or accidentally trapped solid phases were confirmed in multiphase inclusions (diagnostic bands given in brackets): magnetite ( $665 \text{ cm}^{-1}$ ), pyrite ( $341$  and  $376 \text{ cm}^{-1}$ ), chalcopyrite ( $292 \text{ cm}^{-1}$ ), anhydrite ( $611$ ,  $1018$ , and  $1131 \text{ cm}^{-1}$ ), hematite ( $1320 \text{ cm}^{-1}$ ), and siderite ( $1090 \text{ cm}^{-1}$ ; Fig. 11).

#### 4.3. Microthermometry

In the Sarkuh porphyry deposit, almost all of the SH inclusions

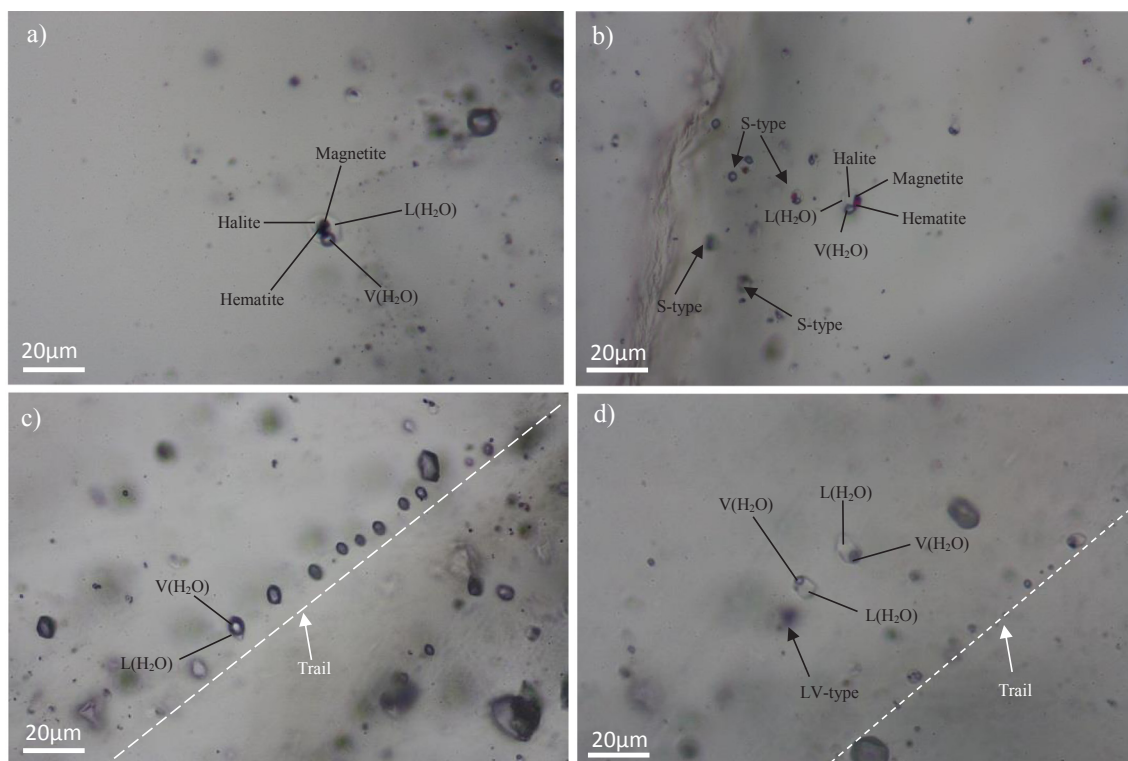


**Fig. 8.** Examples of representative fluid inclusions in the Iju porphyry copper deposit (a) Isolate multiphase inclusion containing halite, magnetite and hematite in the early pre-ore stage; (b) Multiphase inclusions occurring as cluster in the main ore stage; (c–d) Trails of VL and LV inclusions in the late stage of mineralization.

exhibit similar microthermometric characteristic, i.e., halite dissolution before vapor total homogenization. In the early pre-ore stage SH inclusions, total homogenization ( $T_h$ ) is observed at temperatures between 421.6 and 572.3 °C (average 483.2 °C), whereas halite dissolution  $T_m$  (Halite) occurs at lower temperatures between 238.9 °C and 342.3 °C (average 289.5 °C). The corresponding salinities are 34.0–41.6 wt% NaCl eq. (Fig. 12a and d). The final ice-melting temperatures ( $T_m$  (Ice)) of pre-ore stage SM inclusions range from –16.2 °C to –4.2 °C (average –8.4 °C), corresponding to salinities of 6.6–19.5 (average 11.7) wt. % NaCl eq. (Fig. 12d). In these inclusions,  $T_h$  is 490–585 °C (average 534 °C) (Table 2). The obtained first ice melting temperatures ( $T_e$ ) in the SM inclusions range between –21.6 and –55.1, representing the contribution of Na and K cations with other divalent cations including Ca, Fe and Mg in the solution (e.g., Zarasvandi et al., 2015b). The VL inclusions of the early pre-ore stage homogenize at  $T_h$  420–578 °C (average 504 °C), with  $T_m$  (Ice) of –16.2––5.4 °C, corresponding to salinities between 8.3 and 19.6 (average 14.5) wt. % NaCl eq. In three VL inclusions the eutectic temperatures are –21.2, –37.2 and –54.1. The CO<sub>2</sub>-bearing VL inclusions (C-type) have CO<sub>2</sub> triple-phase point of –57 °C (average temperatures of solid CO<sub>2</sub> melting), clathrate melting temperature ranging between 1.9 and 3.4 °C (average 12.1 wt% NaCl eq.), and  $T_h$  between 401 and 542 °C (Fig. 12a and d).

The main ore stage is dominated by SH, SM, and VL inclusions; LV and C-type (VL with CO<sub>2</sub> vapor bubble) inclusions are rare. Most of the SH inclusions homogenize into the liquid phase at  $T_h$  of 345.4–469.6 °C (average 395.4 °C). Halite dissolution  $T_m$  (Halite) occurs at 167.2–334.5 °C (average 265.2 °C), corresponding to salinities of 30.3–41.0 (average 35.8) wt. % NaCl eq. The VL inclusions of the main ore stage homogenize at  $T_h$  362.4–434.9 °C (average 390.8 °C), with  $T_m$  (Ice) –9.7––1.1 °C (average –4.5 °C), corresponding to salinities of 1.0–13.6 wt% NaCl eq. In the main ore stage, the SM inclusions homogenized to or by gas phase or vapor disappearance at  $T_h$  358.2–477.2 °C, with salinities varying between 3.6 and 16.5 wt% NaCl eq. (Fig. 12b, e; Table 2). Late stage quartz veinlets contain mostly SH

and LV inclusions; SM and C-type inclusions are rarely present in some samples. The SH inclusions homogenized by vapor disappearance at  $T_h$  160.8–377.7 °C, and halite dissolution occurs at temperatures of 192.2–244 °C, yielding salinities of 31.4–34.3 wt% NaCl eq. The  $T_h$  values of the late stage LV inclusions are 154.1–315.2 with salinities varying between 0.82 and 14.5 wt% NaCl eq. (Fig. 12c and f). In three LV inclusions the obtained  $T_e$  are –28, –19 and –22.3 °C.

In the early stage of mineralization at Meiduk deposit, majority of SH inclusions (accounting for 55%) homogenized by halite disappearance between 399 and 598 °C (average 498 °C), and calculated salinities (based on halite dissolution temperature) are between 36.4 and 73.2 wt% NaCl eq. VL inclusions of early stage may contain either CO<sub>2</sub> or H<sub>2</sub>O components. The eutectic melting temperatures in the VL inclusions containing CO<sub>2</sub> (C-type) are –59.8––56.6 °C, and CO<sub>2</sub> clathrate melting occurs from 1.1 °C to 2.4 °C, yielding salinities of 12.6–14.3 wt% NaCl eq. The homogenization temperatures of the VL (VH<sub>2</sub>O) inclusions are 429.6–579.2, i.e., similar to those of C-type inclusions (416.1–586.5 °C; Fig. 13a, d). The final ice melting temperatures of these inclusions range between –19.2 and –14.3 °C, corresponding to salinities of 16.9–21.8 wt% NaCl eq. (Fig. 13d; Table 2). The obtained  $T_e$  in one VL inclusion is –29.8 °C. The main mineralization stage at Meiduk contains SH, LV and VL inclusions. Most of the VL inclusions contain a H<sub>2</sub>O vapor phase, only minor contents of CO<sub>2</sub> were detected by laser Raman analysis. SH inclusions have homogenization temperatures between 312 and 480 °C (average 364 °C) and salinities between 37.1 and 48.9 wt% NaCl eq. (Fig. 13b and e). The VL inclusions show total homogenization to the vapor phase between 335.1 and 386.1 °C, with final ice melting from –15.4 to –5.2 °C, corresponding to salinities of 8.1–18.9 wt% NaCl eq. In the main mineralization stage, the  $T_h$  of LV inclusions are 239.8–348.4 °C, with calculated salinities range from 8.2 to 21.3 wt% NaCl eq. (Fig. 13b and e; Table 2). In one LV inclusion the  $T_e$  is –40 °C. The SH inclusions from late stage quartz veinlets homogenize by halite dissolution or vapor disappearance between 247 and 347 °C; salinities are between 33.8 and 44.4 wt% NaCl eq. The LV inclusions are totally homogenized to liquid

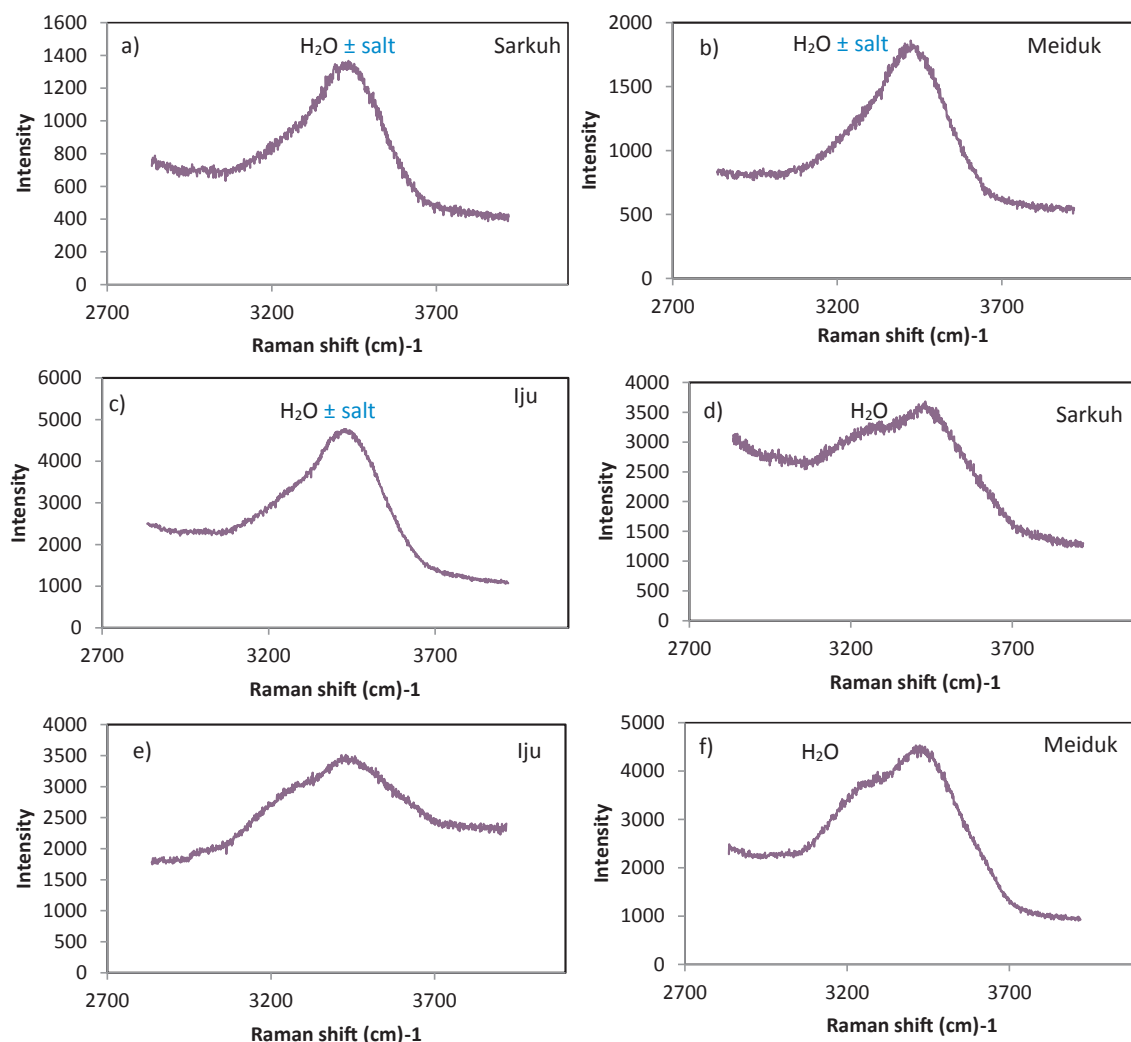


Fig. 9. Laser Raman spectra of liquid phase in LV inclusions. (a–c) Main ore stage; (d–f) Late stage of mineralization.

at temperatures between 272.6 and 357.3 °C; their salinities vary from 1.4 to 16.2 wt% NaCl eq. (Fig. 13c and f; Table 2).

Because we did not find any suitable fluid inclusion ( $< 5\mu\text{m}$ ) in early stage quartz veinlets, we focused on the quartz and quartz-pyrite veinlets of the main and late stage stages. The main stage quartz veinlets contain SH and VL inclusions. The SH inclusions mostly homogenize by vapor disappearance (accounting for 85%) between 438 and 535 °C (average 509 °C). Salinities of these inclusions range between 38.3 and 59.7 (average 46.6) wt.% NaCl eq. (Fig. 14a and c). The VL inclusions homogenize between 450 and 570 °C (average 513 °C), with salinities ranging from 2.1 to 21.8 (average 15.5) wt. % NaCl eq. (Fig. 14a, c; Table 2). Late stage quartz veins contain SH, LV, and VL inclusions with C-type inclusion being rare (Fig. 14b and d). The SH inclusions homogenize either by disappearance of the vapor phase or by halite dissolution at temperatures of 246.0–415.1 °C (average 354.2 °C). Salinities of these inclusions range between 28.4 and 49.1 (average 39.9) wt. % NaCl eq. The homogenization of VL inclusion occurs between 280.1 and 418.5 °C (average 366.2 °C), with ice melting temperatures varying from  $-19.1$  to  $-1.9$  °C, corresponding to salinities of 3.1–21.7 wt% NaCl eq. The LV inclusions homogenize at temperatures of 190.6–387.3 °C (average 344.1 °C); with calculated salinities from 0.82 to 7.9 wt% NaCl eq. In three LV inclusions the obtained  $T_e$  are  $-26.3$ ,  $-41.2$  and  $-51.4$  °C. Two analyzed C-type inclusions exhibit solid  $\text{CO}_2$  melting at  $-56.6$  and  $-57.1$  °C, and clathrate melting at 9.5 and 8.6 °C, respectively. They have salinities of 1.02 and 2.7 wt% NaCl eq. (Fig. 14d).

Three types of fluid inclusions, i.e., SH, VL, and LV have also been identified in the Iju deposit. Quartz veinlets of the ore and late stages contain all the three types of fluid inclusions. In the early stage, the VL inclusions are two-phase (L + V)  $\text{H}_2\text{O}$  inclusion; small amounts of  $\text{CO}_2$  were only detected by laser Raman analysis. In these inclusions, the homogenization temperatures range from 500 to 575.1 °C (average 531.4 °C), and final melting temperature of ice occurs in the interval of  $-20.1$  to  $-9.6$  °C (average  $-15.8$  °C), yielding salinities of 13.5–22.4 wt% NaCl eq. (Fig. 15a and d). The  $T_h$  of SH inclusions (homogenized by vapor disappearance or halite dissolution) is 503.1–590.0 °C (average 562.5 °C), and calculated salinities for these inclusions vary between 42.2 and 71.1 (average 60.9) wt. % NaCl eq. (Fig. 15a and d). The  $T_h$  values of SH inclusions from the ore stage are 391–509 °C (average 455 °C), and the calculated salinities range from 40.4 – 60.9 (average 53.1) wt. % NaCl eq. One LV inclusion yielded ice melting temperature of  $-4.1$  °C (6.5 wt% NaCl eq.) and final homogenization temperature of 495.1 °C. The VL inclusions of this stage, homogenize between 390.1 and 480 °C (average 427.7 °C), with salinities varying between 9.7 and 22.4 wt% NaCl eq. (Fig. 15b, e; Table 2). The LV inclusions are abundant in the late stage, compared with other mineralization stages. They are homogenized in temperatures of 219.3–386.1 °C, having salinities of 0.16–10.6 wt% NaCl eq. In this stage, total homogenization temperatures of SH inclusions range between 263 and 410 °C (average 344 °C) and their salinities are between 33.4 and 48.5 wt% NaCl eq. The gas homogenization for VL inclusions is between 326 and 394.1 °C (average 357.8 °C), with ice melting



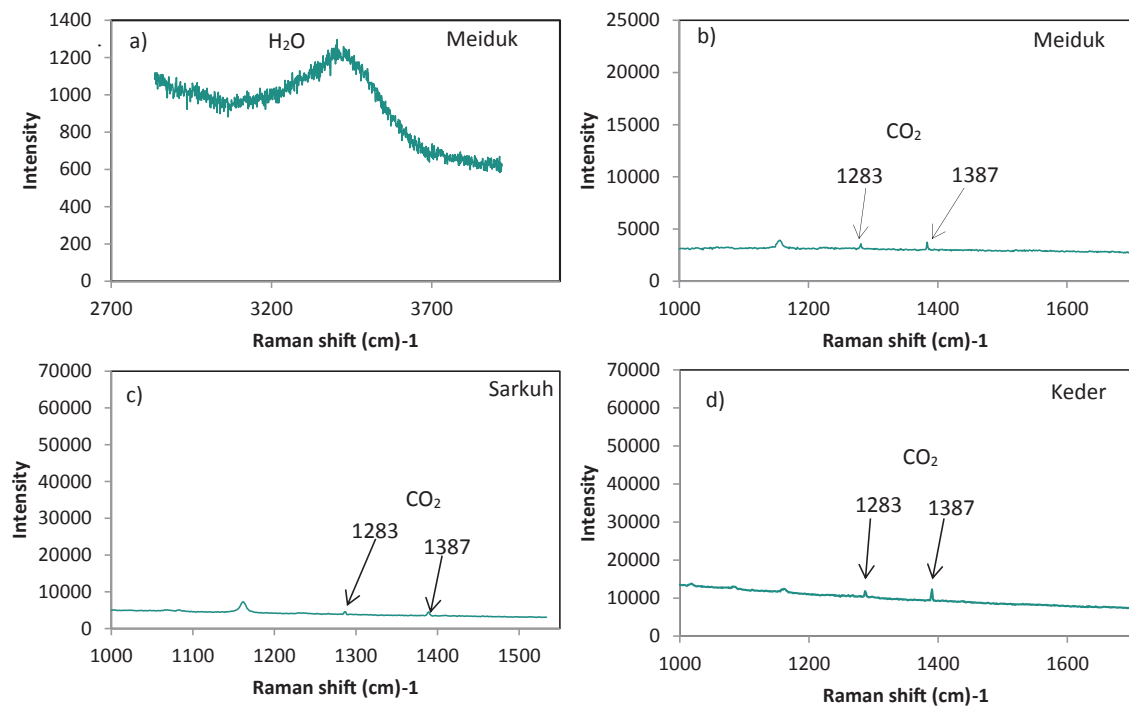


Fig. 10. Laser Raman spectra of vapour phase in VL inclusions. (a–b) Early stage; (c–d) Main and late stages of mineralization, respectively.

temperatures ranging from  $-12.5$  to  $-1.7$  °C, corresponding salinities of 2.7–16.4 wt% NaCl eq. (Fig. 15c and f).

## 5. Discussion

### 5.1. Nature of initial hydrothermal fluids

As a common indication, halite-saturated aqueous inclusions (containing halite cube) were reported from many porphyry copper deposits, especially in the early-stages of the hydrothermal evolution (e.g., Pirajno, 2009; Yang et al., 2015). But saturation with NaCl is not the typical feature of the primary magmatic fluids. At deep emplacement of

porphyry intrusions low saline NaCl-poor magmatic-hydrothermal fluids are initially exsolved from the magmas (e.g., Baker, 2002). Examples of this are the Qian'echong porphyry Mo deposit (Fei Yang et al., 2013) or the Butte porphyry Cu-Mo system that was emplaced at depths down to 9 km with the initial hydrothermal fluids only having 2–10 wt % NaCl eq. (Rusk et al., 2008; Sillitoe, 2010). Importantly, besides depth, the exact composition of exsolved magmatic volatile phases may depend on many other variables, i.e., initial magmatic Cl/H<sub>2</sub>O ratios and alkali content (Richards, 2011). As depicted in Giggensbach (1997), exsolution pressure of Cl from magma is lower than CO<sub>2</sub> and H<sub>2</sub>O resulting in first generation of low-salinity CO<sub>2</sub>-rich fluids at depth. In contrast, shallowly emplaced magmas generally exhibit high salinity

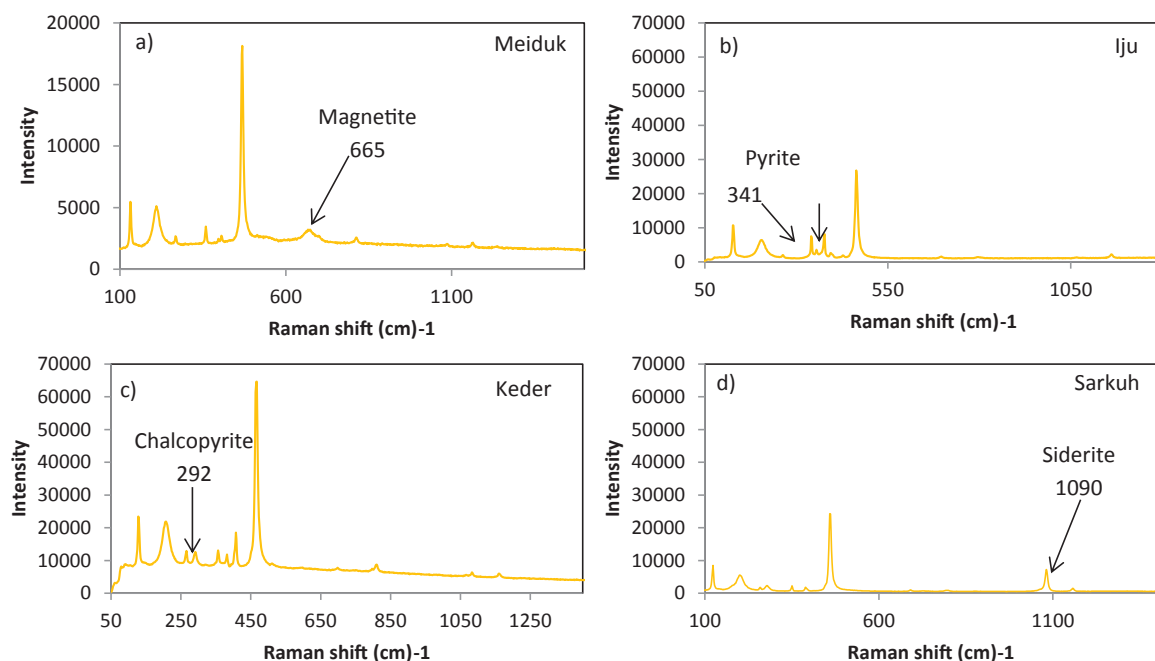


Fig. 11. Laser Raman spectra of solid phases found in the multiphase fluid inclusions. See text for explanations.

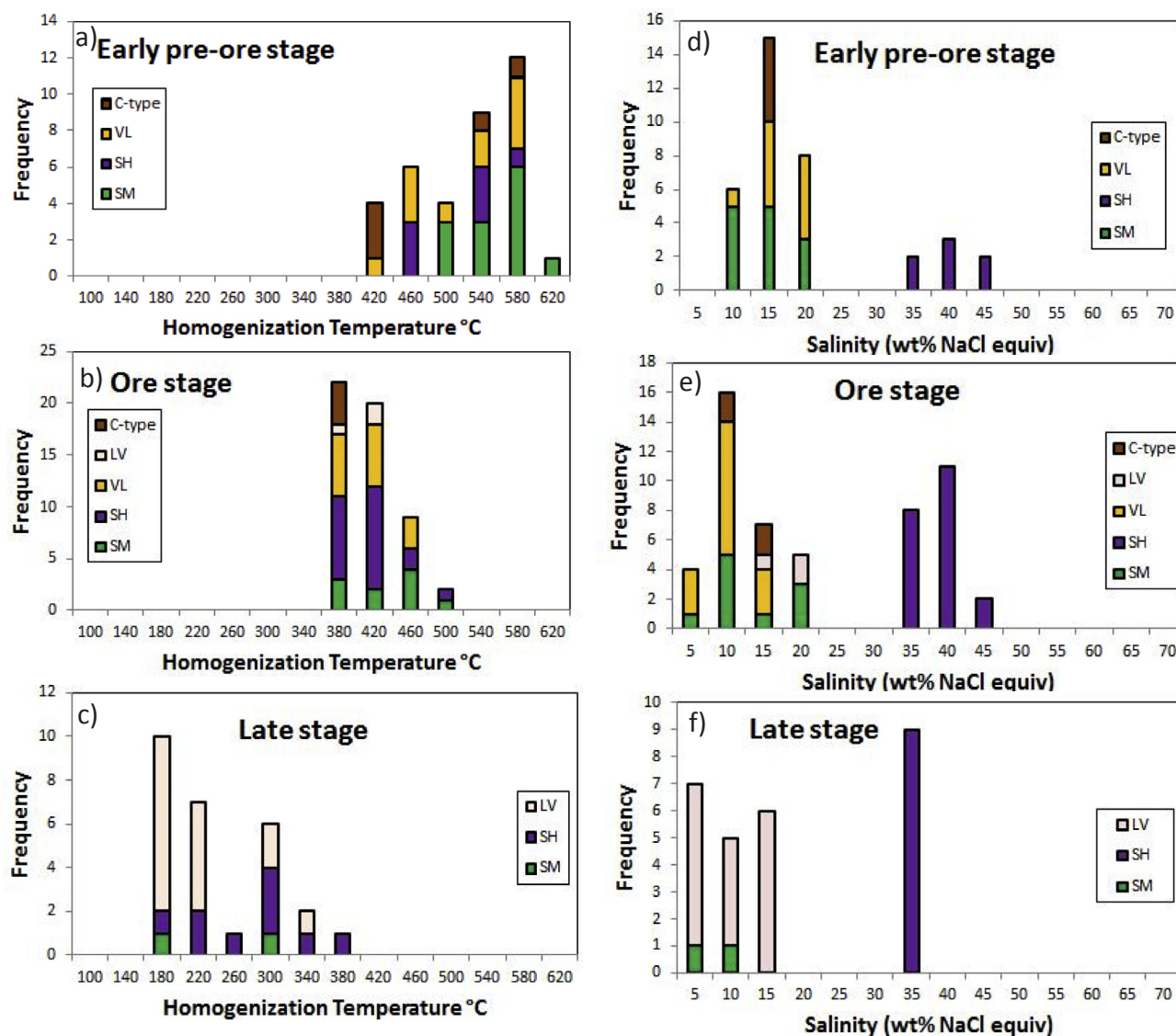


Fig. 12. Histograms showing  $T_h$  °C (a–c) and salinities of fluid inclusions (d–f) from the three stages, Sarkuh deposit. For explanation of fluid inclusion types see text.

brine and immiscible low salinity vapor in early exsolved fluids (Lowenstern, 2001; Richards, 2011).

As in many other shallowly emplaced porphyry systems, the initial early or pre-ore stages in all the studied Iranian porphyry copper deposits is characterized by the presence of halite-saturated inclusions (SH-type). Upon heating, halite-saturated inclusions exhibit three different modes of homogenization (Becker and Bodnar, 2008), including: (1) simultaneous disappearance of halite with bubble or liquid homogenization ( $T_h(\text{Halite}) = T_h(L - v)$ ); (2) priority of halite disappearance compared with vapor or liquid homogenization ( $T_h(\text{Halite}) < T_h(L - v)$ ); and (3) vapor–liquid homogenization before halite dissolution ( $T_h(\text{Halite}) > T_h(L - v)$ ). Our microthermometric results for the early quartz veinlets reveal that the majority of SH inclusions in the smaller and lower grade porphyry deposits, such as Sarkuh and Iju, exhibit halite dissolution before total vapor–liquid homogenization (mode 2 of Becker and Bodnar, 2008). In contrast, inclusions entrapped in the early quartz veinlets of Meiduk porphyry copper system are mostly showing NaCl supersaturation, expressed as halite dissolution after liquid-vapor homogenization (mode 3). This feature is interpreted to be related to the homogeneous trapping of inclusion during high pressure conditions (Bodnar, 1994) or it may be due to the inhomogeneous trapping of halite-saturated hydrothermal brines (Becker and Bodnar, 2008; Yang

et al., 2015; Zarasvandi et al., 2015b; Liu et al., 2016). It is important to note that post-entrapment processes (e.g., volume shrinkage, loss of  $H_2O$ , stretching and necking) can also cause NaCl supersaturation in SH inclusions (Sterner et al., 1988; Becker and Bodnar, 2008; Shen et al., 2010; Yang et al., 2015; Zarasvandi et al., 2015b). No signs of post-entrapment modifications were, however, observed during petrographic examinations of the fluid inclusions. The co-occurrence of SH inclusions with type- III homogenization (homogenization by halite disappearance) and vapor-rich inclusions in the most primitive veins of highly mineralized Meiduk deposit provide direct evidence for halite saturation along the liquid-vapor-halite curve, analogous to those reported from other porphyry copper systems (Lecumberri-Sanchez et al., 2015; Wang et al., 2017).

Based on the phase identification using laser Raman analysis, the primitive multiphase inclusions (those hosted in early stage quartz veinlets) in the highly mineralized Meiduk deposit contain significant co-occurrence of magnetite, hematite as well as anhydrite daughter phases, implying for oxidized conditions of early stages of hydrothermal system (Wang et al., 2017). These solid phases are less common in the smaller and lower grade deposits (i.e., Iju). As stated above, recent findings indicate that the Miocene porphyries of UDMB are mostly produced by partial melting of thickened mafic lower crust. According

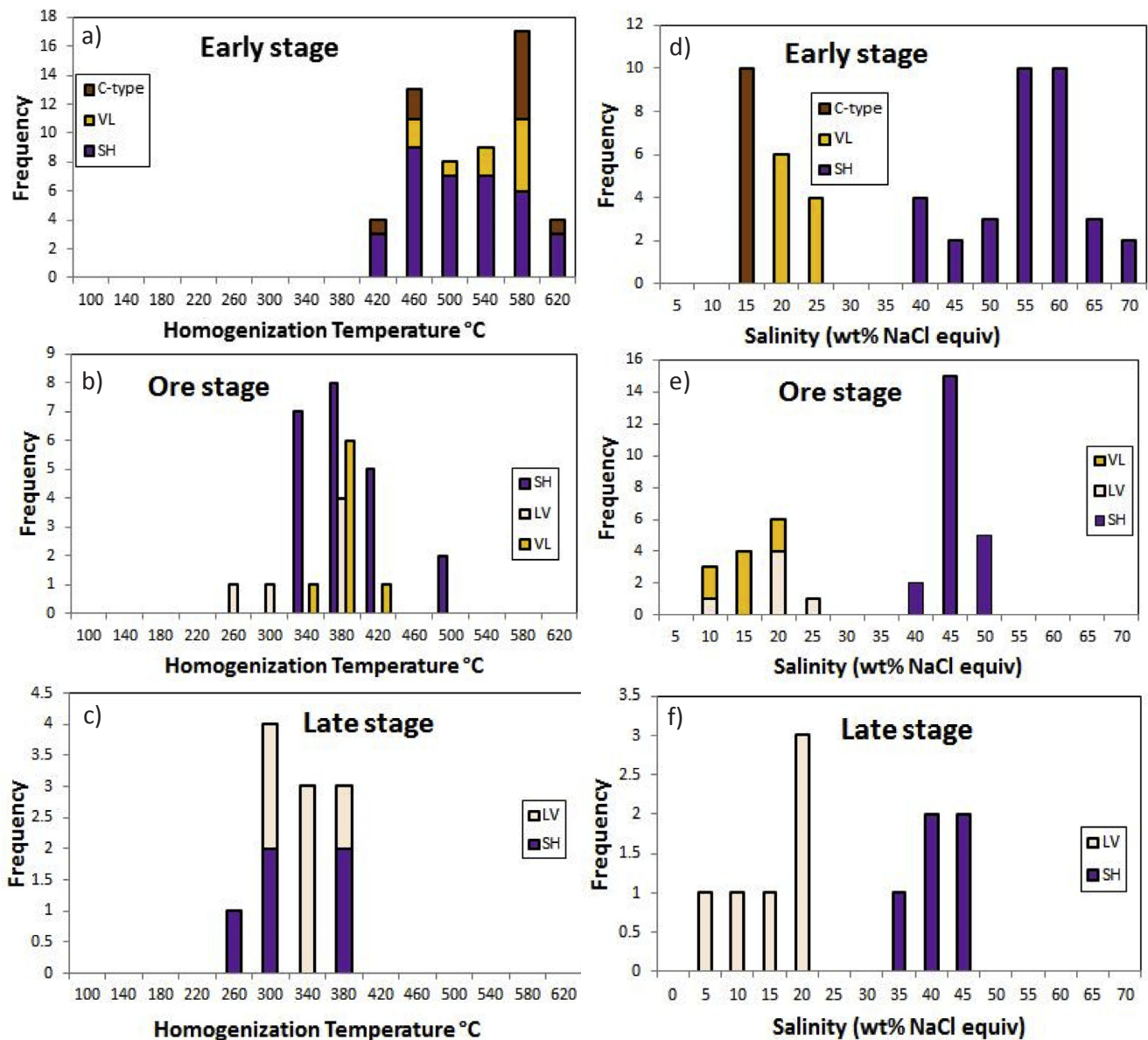


Fig. 13. Histograms showing  $T_h$  °C (a–c) and salinities of fluid inclusions (d–f) from the three stages, Meiduk deposit.

to this model ongoing compression and tectonic shortening after subduction of the Neo-Tethys lead to the development of a garnet amphibolite melting zone in the lower crust during continent–continent collision providing the source of the magmas (Shafiei et al., 2009; Asadi et al., 2014; Zarasvandi et al., 2015a,b, 2018). Collisional porphyry copper deposits derived from the partial melting of such thickened juvenile mafic lower crust generate relatively oxidized magmatic systems. The oxygen fugacities ( $fO_2$ ) of these magmas are  $\Delta FMQ + 2$  (where FMQ is the fayalite–magnetite–quartz oxygen buffer) reaching up to  $\Delta FMQ + 4$ , i.e., close to the magnetite–hematite oxygen (MH) buffer (Sun et al., 2015). The presence of magnetite, hematite, and anhydrite in the multiphase inclusions entrapped in the early veins (e.g., Meiduk porphyry) prove that oxygen fugacity of the hydrothermal system fluctuated near the MH buffer (Sun et al., 2013). Importantly, the oxidized nature of the magmas and the early stage hydrothermal fluids expelled from them would provide suitable conditions for the preservation of sulfur content. Because under oxidized conditions,  $H_2S$  will be undersaturated and tend not to be fractionated from magmatic-hydrothermal system leading to the preservation of sulfur and chalcophile

elements of hydrothermal system (Richards, 2011; Sun et al., 2013). Accordingly, early quartz veinlets associated with potassic alteration do not contain considerable sulfide mineralization (Fig. 4).

## 5.2. Evolution of hydrothermal system and sulfide mineralization

Fig. 16 shows plots of  $T_h$  °C versus salinity of the various fluid inclusions entrapped in the early, main ore, as well as late stages of hydrothermal system for the four studied deposits. The diagram shows that from the early to the late stage, there is a gradual decrease in  $T_h$  °C with large variations in salinity (Fig. 16). As a common indication in the porphyry copper systems, this feature is attributed to the inflow or mixing of early hypersaline high-temperature magmatic fluids with circulating groundwater (e.g., Gregory, 2017; Yu et al., 2017). Through hydrothermal evolution, this is generally accompanied with the developing of hydraulic fracturing and fluid boiling (Canet et al., 2011; Dubessy et al., 2003; Zarasvandi et al., 2015b; Fig. 16).

It is evident that homogenization temperatures of ore stage fluid inclusions in the lower grade deposits Sarkuh, Iju and Keder are higher



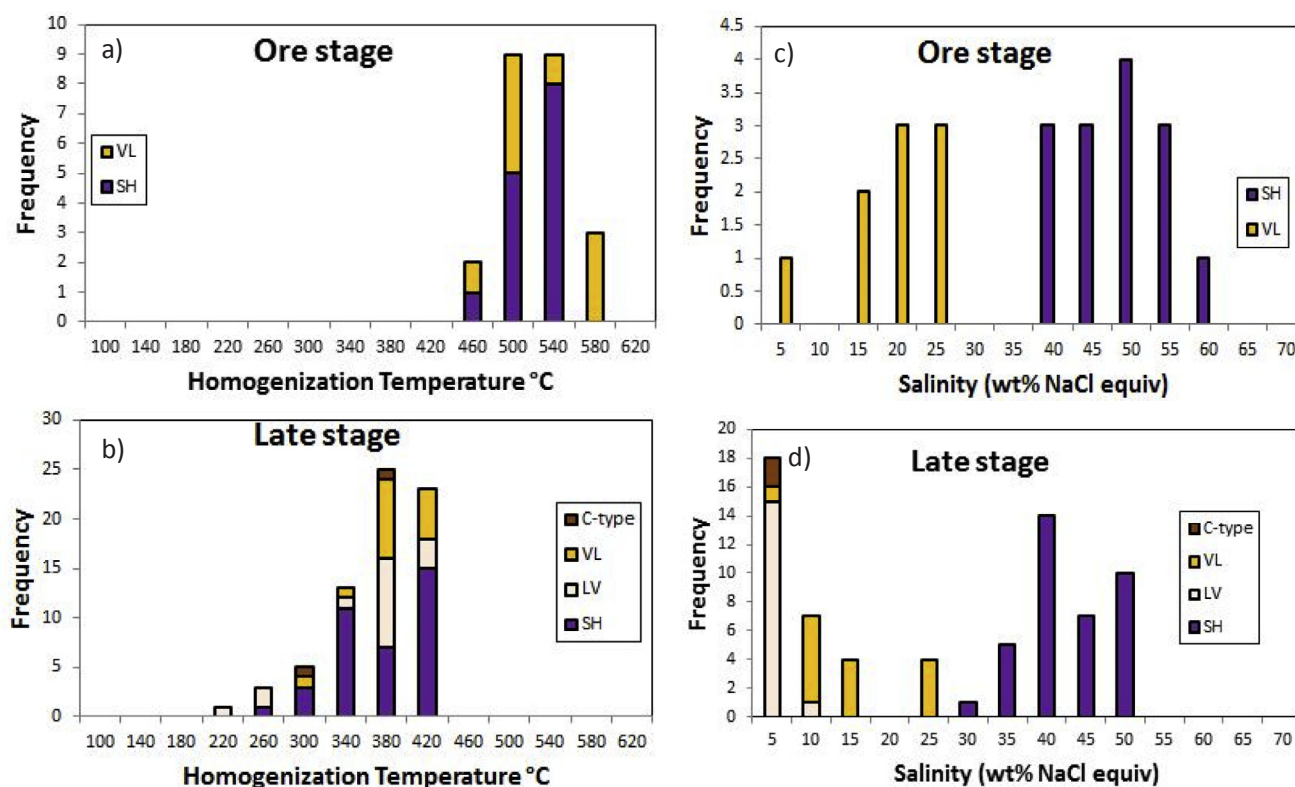
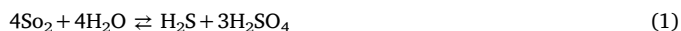


Fig. 14. Histograms showing  $T_h$  °C (a–b) and salinities of fluid inclusions (c–d) from the ore stage and late stage, Keder deposit.

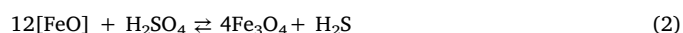
than those in the large higher grade Meiduk deposit (Fig. 16). For example,  $T_h$  °C values of ore stage SH inclusions increase on average from Meiduk (364.1 °C) to Sarkuh (395.4 °C), Iju (455.2 °C) and Keder (508.7 °C). This feature may highlight the important role of temperature decrease for sulfide saturation/mineralization. As explained above, the oxidized nature of the magma and initial hydrothermal fluids plays a decisive role in keeping the sulfur content high, therefore restricting sulfide segregation during the magmatic and early hydrothermal stages (Yang, 2012; Sun et al., 2013). However, the availability of reduced sulfur species ( $\text{HS}^-$ ,  $\text{H}_2\text{S}$ ) is crucial for forming major sulfide mineralization in the main ore stage of porphyry copper systems. Decrease in temperature has a major effect on the disproportionation of dissolved oxidized sulfur species ( $\text{SO}_2$ ) to hydrogen sulfide ( $\text{H}_2\text{S}$ ) and  $\text{H}_2\text{SO}_4$  (eq. (1); Richards, 2011).



Cooling of the hydrothermal system is shifting this reaction to the right side thus providing hydrogen sulfide necessary for the generation of sulfide mineralization in the main ore stage (Richards, 2011; Zarasvandi et al., 2018). The production of  $\text{H}^+$  during this reaction decreasing the pH, providing suitable conditions for hydrolysis and wall rock alteration (towards neutralization). This mechanism could explain why ore stage veinlets containing significant sulfide mineralization generally have a sericite halo in which feldspar is altered (Fig. 4b).

Based on laser Raman spectroscopy analysis, it is shown that inclusions with signs of  $\text{CO}_2$  components (in vapor phase) are present in the hydrothermal systems of almost all studied porphyry copper deposits (Fig. 10b–d). It is most common in the early stage quartz veinlets at Meiduk (C-type inclusions). As noted earlier, the abundance of  $\text{CO}_2$  vapor components decrease from early to late stage quartz veinlets. Nevertheless, in the Meiduk deposit this decreasing trend is much higher than that of other deposits. Aside from porphyry Mo deposits (e.g., Qian'echong, Fei Yang et al., 2013; Yuchiling, Li et al., 2012),  $\text{CO}_2$ -bearing fluid inclusions have also been reported from porphyry Cu

systems, especially those formed in continental collision/post-collisional tectonic regimes (e.g., Dalli porphyry Cu-Au deposit, Urumieh-Dokhtar magmatic belt, Zarasvandi et al., 2015b; Dabu porphyry Cu-Mo deposit, southern Tibet; Wu et al., 2017), and when porphyry Cu systems were deeply emplaced (e.g., Butte porphyry Cu-Mo deposit; Rusk et al., 2008; Liu et al., 2016). Totally,  $\text{CO}_2$  components may have a decisive role in metal transportation/deposition by buffering the ore-bearing fluids (Phillips and Evans, 2004). For example, experimental results have indicated that without significant contribution from the brine, the  $\text{CO}_2$ -rich magmatic vapor components could remove half of the available copper from the melt (Tattitch et al., 2015). Also, in more saline oxidizing and S-rich fluids as generally seen in PCDs, the solubility of ore metals (Cu-Au-Fe) in the presence of  $\text{CO}_2$  decrease by ~ 1 order of magnitude with  $\text{CO}_2$  increasing to 20–30 wt% (Kokh et al., 2017). Because of the low solubility of  $\text{CO}_2$  in magmas compared to  $\text{H}_2\text{O}$ ,  $\text{CO}_2$  tends to be exsolved in the very early magmatic-hydrothermal stage (differential degassing), i.e., the earliest fluids are usually relatively  $\text{CO}_2$ -rich (Drummond and Ohmoto, 1985; Chen and Wang, 2011; Liu et al., 2016). This may explain the decrease of  $\text{CO}_2$  vapor components with decreasing temperature from early to late stages as seen in the Meiduk porphyry. It should be noted that besides cooling three other mechanisms are considered as important factor for changing the oxidation state of the hydrothermal system. 1) magnetite crystallization (eq. (2), Liang et al., 2009; Sun et al., 2013), 2)  $\text{CO}_2$ -escape by boiling (Li et al., 2012; Zhong et al., 2014), and 3) differential  $\text{H}_2$  escape in the subvolcanic venting environment.



In the early stages of hydrothermal system during potassic alteration, magnetite crystallization could facilitate the progressive reduction of  $\text{SO}_4^{2-}$  to  $\text{S}^{2-}$ , providing suitable condition for significant sulfide mineralization in the main stages of mineralization (eq. (2); Liang et al., 2009; Wang et al., 2016). On the other hand,  $\text{CO}_2$ -escape would also increase the pH in the remaining fluids making Cu-Cl and Au-Cl

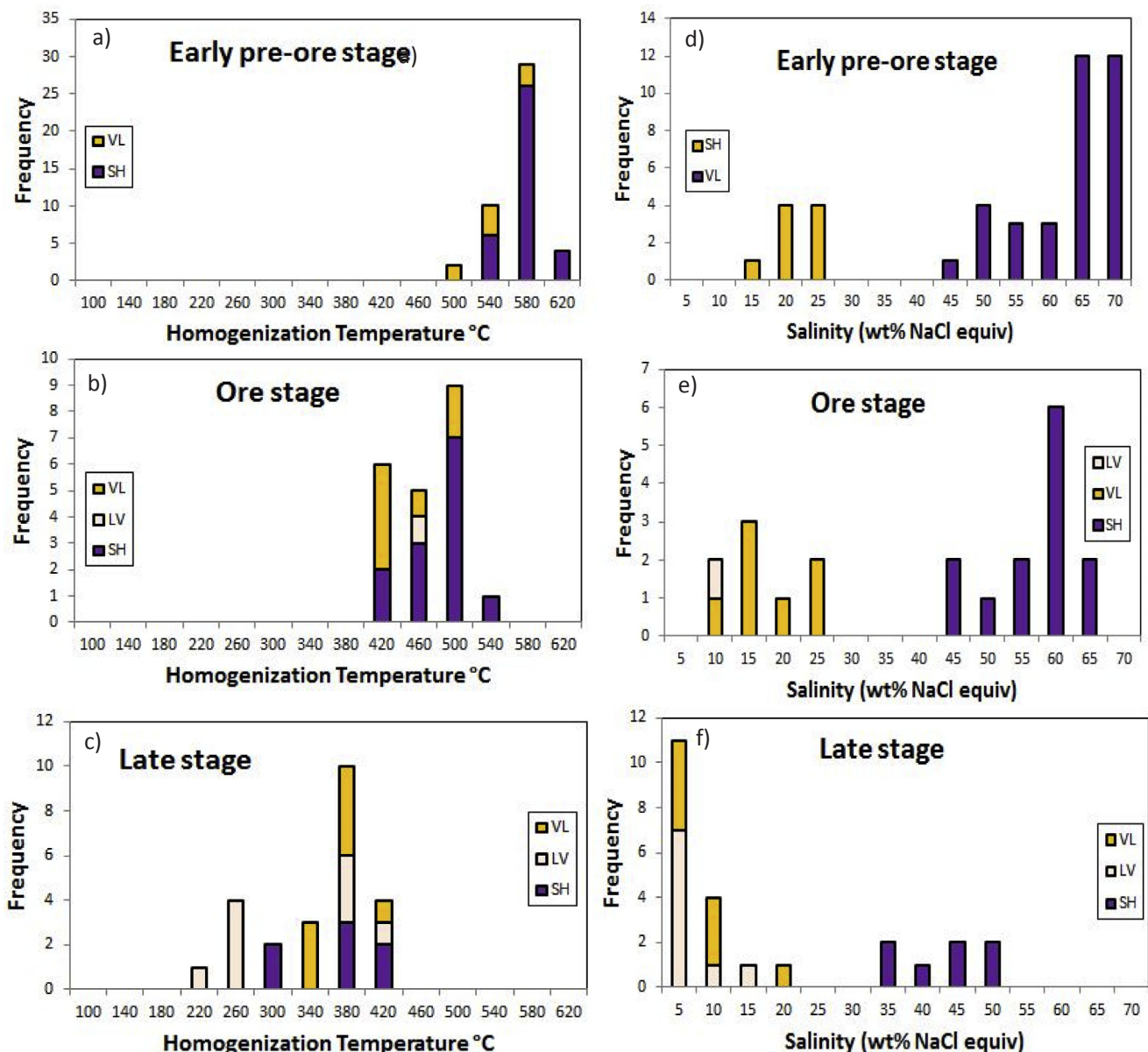


Fig. 15. Histograms showing homogenization temperatures (a–c) and salinities of fluid inclusions (d–f) from the three stages, Iju deposit.

complexes less soluble and could be linked directly to the potential of hydrothermal system for considerable sulfide mineralization (Gammons and Williams-Jones, 1997; Robb, 2005). Thus, CO<sub>2</sub> differential degassing together with cooling of the system could be considered as the main processes of sulfate reduction causing the formation of reduced sulfur species and main ore stage sulfide mineralization. Loss of CO<sub>2</sub> decreases carbonic acid as well, which can increase pH slightly. However, this is also the case for SO<sub>2</sub> and H<sub>2</sub>SO<sub>4</sub> (i.e., partially affected by differential degassing) as well that reduces total S in the magmatic hydrothermal system, so ferrous Fe (Cu, Au) in the magmatic and fluid system also needs to act to enhance that reduction process (i.e., a high Fe; Yang, 2012).

Comparing the overall features of hydrothermal system in the highly mineralized Meiduk deposit with giant Dexing porphyry Cu–Mo–Au deposit in the south China block (Liu et al., 2016) indicate that the signals of high metal fertility, i.e., exhausting of CO<sub>2</sub> components through evolution of hydrothermal system, supersaturation of NaCl in the most primitive fluids, and temperature decreasing during mineralization stages (~300–400 °C) as non-unique factors could also

be seen in the other PCDs repressing anomalously high mineralization.

## 6. Conclusions

In the present work, it is tried to characterize the hydrothermal system of the collisional porphyry copper systems (Meiduk, Iju, Sarkuh, and Keder) located in the Urumieh-Dokhtar Magmatic Belt. Of these deposits, Meiduk is a highly mineralized large economic deposit, whereas Keder represents the low grade sub-economic endmember. Comparing the common characteristics of the hydrothermal system and its evolution from initial stages toward main sulfide mineralization, and late stages, it is proved that the enhancement of metal fertility in the collisional porphyry copper systems could be predicted by the following signals:

- 1) The composition of early hydrothermal fluids; maximum ore-efficiently appear to be accompanied with porphyry deposits representing supersaturation of NaCl in the most primitive fluids (e.g., Meiduk deposit: 36.4–73.2 wt% NaCl eq.).

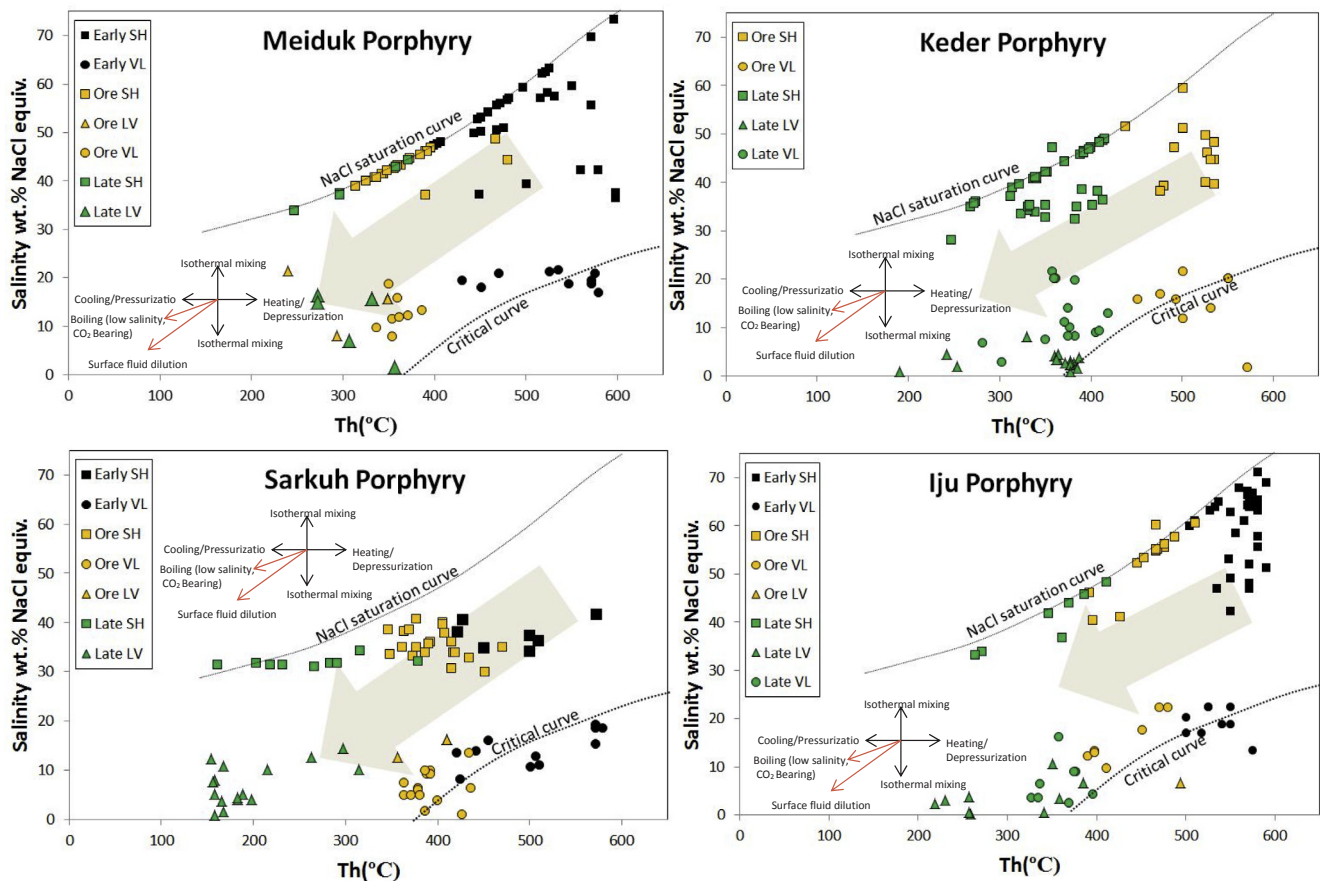


Fig. 16.  $T_h$  °C vs. salinity of fluid inclusions from the different stages of mineralization for the four porphyry deposits studied (diagram with critical curve and NaCl saturation curve is after Bodnar, 1983). The gray arrow indicates the trend of decreasing in homogenization and salinity. Evolutionary paths of hydrothermal fluid are from Wilkinson (2001).

- 2) Oxygen fugacity of the magmatic-hydrothermal system; high  $fO_2$  as indicated by presence of magnetite, hematite, and anhydrite especially in the pre-ore stage inclusions favor high sulfur (and metal) contents in the hydrothermal fluids of the main ore stage.
- 3) Presence of  $CO_2$  as fluid component and loss of  $CO_2$  in the low density volatile (vapor) phase during the evolution of system.
- 4) Temperature decrease, especially during the transition from the pre-ore/early ore to the main ore stage.

For the formation of large to giant high-grade porphyry copper deposits, the processes controlling these parameters must be ideally combined. If not, only low-grade sub-economic systems will develop.

## Acknowledgements

This research was made possible by the grant of the office of vice-chancellor for research and technology, Shahid Chamran University of Ahvaz in 2017–2018. We acknowledge their supports. The second author expresses his appreciation to Professor Ronald Bakker for facilitating the contribution in the fluid inclusion short course at Montanuniversität Leoben, and valuable practical guidance during fluid inclusion and laser Raman spectroscopy analyses.

## References

Aghazadeh, M., Hou, Z., Badrzadeh, Z., Zhou, L., 2015. Temporal-spatial distribution and tectonic setting of porphyry copper deposits in Iran: constraints from zircon U-Pb and molybdenite Re-Os geochronology. *Ore Geol. Rev.* 70, 385–406.  
 Alavi, M., 2007. Structures of the Zagros fold-thrust belt in Iran. *Am. J. Sci.* 307, 1064–1095.

Asadi, S., Moore, F., Zarasvandi, A., 2014. Discriminating productive and barren porphyry copper deposits in the southeastern part of the central Iranian volcano-plutonic belt, Kerman region, Iran: a review. *Earth Sci. Rev.* 138, 25–46.  
 Audetat, A., Pettke, T., Heinrich, C.A., Bodnar, R., 2008. The composition of magmatic-hydrothermal fluids in barren and mineralized intrusions. *Econ. Geol.* 103, 877–908.  
 Baker, T., 2002. Emplacement depth and carbon dioxide-rich fluid inclusions in intrusion-related gold deposit. *Econ. Geol.* 97, 1111–1117.  
 Becker, S.P., Bodnar, R.J., 2008. Synthetic fluid inclusions. XVII. PVTX properties of high salinity  $H_2O$ -NaCl solutions (> 30 wt% NaCl): application to fluid inclusions that homogenize by halite disappearance from porphyry copper and other hydrothermal ore deposits. *Econ. Geol.* 103, 539–554.  
 Berberian, F., Muir, I.D., Pankhurst, R.J., Berberian, M., 1982. Late Cretaceous and early Miocene Andean type plutonic activity in northern Makran and central Iran. *J. Geol. Soc.* 139, 605–614.  
 Blundy, J., Mavrogenes, J., Tattitch, B., Sparks, S., Gilmer, A., 2015. Generation of porphyry copper deposits by gas-brine reaction in volcanic arcs. *Nat. Geosci.* <https://doi.org/10.1038/NGEO2351>.  
 Bodnar, R.J., 1983. A method of calculating fluid inclusion volumes based on vapor bubble diameters and PVTX properties of inclusion fluid. *Econ. Geol.* 78, 535–542.  
 Bodnar, R.J., 1994. Synthetic fluid inclusions. XII. The system  $H_2O$ -NaCl. Experimental determination of the halite liquidus and isochores for a 40 wt% NaCl solution. *Geochim. Cosmochim. Acta* 58, 1053–1063.  
 Canet, C., Franco, S.I., Prol-Ledesma, R.M., González-Partida, E., Villanueva-Estrada, R.E., 2011. A model of boiling for fluid inclusion studies: application to the Bolaños Ag-Au-Pb-Zn epithermal deposit, Western Mexico. *J. Geochem. Explor.* 110, 118–125.  
 Chelle-Michou, C., Rottier, B., Caricchi, L., Simpson, G., 2017. Tempo of magma degassing and the genesis of porphyry copper deposits. *Nat. Geosci.* 7, 40566. <https://doi.org/10.1038/srep40566>.  
 Chen, Y.J., Wang, Y., 2011. Fluid inclusion study of the Tangjiaping Mo deposit, Dabie Shan, Henan Province: implications for the nature of porphyry systems of postcollisional tectonic settings. *Int. Geol. Rev.* 53, 635–655.  
 Drummond, S.E., Ohmoto, H., 1985. Chemical evolution and mineral deposition in boiling hydrothermal systems. *Econ. Geol.* 80, 126–147.  
 Dubessy, J., Derome, D., Sausse, J., 2003. Numerical modeling of fluid mixings in the  $H_2O$ -NaCl system application to the North Caramal U prospect (Australia). *Chem. Geol.* 194, 25–39.  
 Fei Yang, Y., Chen, Y.J., Li, N., Mi, M., Xu, Y.L., Li, F.L., Wan, S.Q., 2013. Fluid inclusion



- and isotope geochemistry of the Qian'echong giant porphyry Mo deposit, Dabie Shan, China: a case of NaCl-poor, CO<sub>2</sub>-rich fluid systems. *J. Geochem. Explor.* 124, 1–13.
- Frezzotti, M.L., Tecce, F., Casagli, A., 2012. Raman spectroscopy for fluid inclusion analysis. *J. Geochem. Explor.* 112, 1–20.
- Gammons, G.H., Williams-Jones, A.E., 1997. Chemical mobility of gold in the porphyry-epithermal environment. *Econ. Geol.* 92, 45–59.
- Ghorbani, M., Ebrahimi, M., 2009. Tertiary-quaternary magmatism in the Dehaj area. *Earth Recourse J.* 1, 77–89.
- Giggenbach, W.F., 1997. The origin and evolution of fluids in magmatic-hydrothermal systems. In: Barnes, H.L. (Ed.), *Geochemistry of Hydrothermal Ore Deposits*. John Wiley and Sons Inc., New York, pp. 737–796.
- Golestani, M., Karimpour, M.H., Malekzadeh Shafaroudi, A., Haidarian Shahri, M.R., 2018. Geochemistry, U-Pb geochronology and Sr-Nd isotopes of the Neogene igneous rocks, at the Iju porphyry copper deposit, NW Shahr-e-Babak, Iran. *Ore Geol. Rev.* 93, 290–307.
- Gregory, M.J., 2017. A fluid inclusion and stable isotope study of the Pebble porphyry copper-gold-molybdenum deposit, Alaska. *Ore Geol. Rev.* 80, 1279–1303.
- Hassanzadeh, J., 1993. Metallogenic and tectonomagmatic events in the SE sector of the Cenozoic active continental margin of central Iran (Shahr-e Babak area, Kerman Province). Ph.D thesis. University of California, Los Angeles.
- Hezarkhani, A., Williams-Jones, A.E., 1998. Controls of alteration and mineralization in the Sungun porphyry copper deposit, Iran: evidence from fluid inclusions and stable isotopes. *Econ. Geol.* 93, 651–670.
- Kokh, M.A., Akinfiev, N.N., Pokrovski, G.S., Salvi, S., Guillaume, D., 2017. The role of carbon dioxide in the transport and fractionation of metals by geological fluids. *Geochim. Cosmochim. Acta* 197, 433–466.
- Lecumberri-Sanchez, P., Steele-MacInnis, M., Weis, P., Driesner, T., Bodnar, R.J., 2015. Salt precipitation in magmatic-hydrothermal systems associated with upper crustal plutons. *Geology* 43, 1063–1066.
- Li, N., Ulrich, T., Chen, U.J., Thomsen, T.B., Pease, V., Pirajno, F., 2012. Fluid evolution of the Yuchiling porphyry Mo deposit, East Qinling, China. *Ore Geol. Rev.* 48, 442–459.
- Liang, H.Y., Sun, W.D., Su, W.C., Zartman, R.E., 2009. Porphyry copper-gold mineralization at Yulong, China, promoted by decreasing redox potential during magnetite alteration. *Econ. Geol.* 104, 587–596.
- Liu, X., Fan, H., Hu, F.F., Yang, K.F., Wen, B.J., 2016. Nature and evolution of the ore-forming fluids in the giant Dexing porphyry Cu–Mo–Au deposit, southeastern China. *J. Geochem. Explor.* 171, 83–95.
- Lowenstern, J.B., 2001. Carbon dioxide in magmas and implications for hydrothermal systems. *Miner. Deposita* 36, 490–502.
- McInnes, B.I.A., Evans, N.J., Fu, F.Q., Garwin, S., Belousova, E., Griffin, W.L., Bertens, A., Sukama, D., Permanadewi, S., Andrew, R.L., Deckart, K., 2005. Thermal history analysis of selected Chilean, Indonesian, and Iranian porphyry Cu–Mo–Au deposits, in: Porter, T.M. (Ed.), *Super, Porphyry Copper and Gold Deposits: A Global Perspective*, 1st. PGC Publishing, Adelaide, pp. 1–16.
- Mirnejad, H., Mathur, R., Hassanzadeh, J., Shafie, B., Nourali, S., 2013. Linking Cu mineralization to host porphyry emplacement: Re–Os ages of molybdenites versus U–Pb ages of zircons and sulfur isotope compositions of pyrite and chalcopyrite from the Iju and Sarkuh porphyry deposits in Southeast Iran. *Econ. Geol.* 108, 861–870.
- Mohajjel, M., Fergusson, C.L., Sahandi, M.R., 2003. Cretaceous-Tertiary convergence and continental collision, Sanandaj-Sirjan Zone, western Iran. *J. Asian Earth Sci.* 21, 397–412.
- Nourali, S., 2011. Mineralization modeling and genesis of Sarkuh porphyry copper deposit, Kerman. M.Sc thesis. University of Tehran.
- Nourali, S., Mirnejad, H., 2012. Hydrothermal evolution of the Sarkuh porphyry copper deposit, Kerman, Iran: a fluid inclusion and sulfur isotope investigation. *Geopersia* 2, 93–107.
- Phillips, G.N., Evans, K.A., 2004. Role of CO<sub>2</sub> in the formation of gold deposits. *Nat. Geosci.* 429, 860–863.
- Pirajno, F., 2009. Hydrothermal processes and mineral systems. In: *Geological Survey of Western Australia*. Springer, pp. 1250.
- Rezaei, M., 2017. Effective parameters in mineralization potential of economic and sub-economic porphyry copper deposits in Urumieh–Dokhtar magmatic zone: using geochemical and fluid inclusion studies. Ph.D thesis. Shahid Chamran University of Ahvaz.
- Richards, J.P., 2011. Magmatic to hydrothermal metal fluxes in convergent and collided margins. *Ore Geol. Rev.* 40, 1–26.
- Richards, J.P., 2013. Giant ore deposits formed by optimal alignments and combinations of geological processes. *Nat. Geosci.* 6, 911–916.
- Richards, J.P., 2015a. Introduction to special issue: magmatic and metallogenic evolution of the Tethyan Orogen. *Ore Geol. Rev.* 70, 321–322.
- Richards, J.P., 2015b. Tectonic, magmatic, and metallogenic evolution of the Tethyan orogen: from subduction to collision. *Ore Geol. Rev.* 70, 323–345.
- Richards, J.P., 2016. Clues to hidden copper deposits. *Nat. Geosci.* 9, 1–2.
- Richards, J.P., Spell, T., Rameh, E., Raziq, A., Fletcher, T., 2012. High Sr/Y magmas reflect arc maturity, high magmatic water content, and porphyry Cu ± Mo ± Au potential: examples from the Tethyan arcs of Central and Eastern Iran and Western Pakistan. *Econ. Geol.* 107, 295–332.
- Ricou, L.E., 1994. Tethys reconstructed: plates continental fragments and their boundaries since 260 Ma from Central America to south-eastern Asia. *Geodin. Acta* 7, 169–218.
- Robb, L., 2005. Introduction to ore-forming processes. Blackwell Publishing, London.
- Roedder, E., 1979. Origin and significance of magmatic inclusions. *Bull. Mineral.* 102, 467–510.
- Rusk, B.G., Reed, M.H., Dilles, J.H., 2008. Fluid inclusion evidence for magmatic-hydrothermal fluid evolution in the porphyry copper-molybdenum deposit at Butte, Montana. *Econ. Geol.* 103, 307–334.
- Shafiei, B., Haschke, M., Shahabpour, J., 2009. Recycling of orogenic arc crust triggers porphyry Cu mineralization in Kerman Cenozoic arc rocks, southeastern Iran. *Miner. Deposita* 44, 265–283.
- Shafiei, B., Shahabpour, J., 2008. Gold distribution in porphyry copper deposits of Kerman region, southeastern Iran. *J. Sci. Islamic Republic of Iran* 19, 247–260.
- Shen, P., Shen, Y., Wang, J., Zhu, H., Wang, L., Meng, L., 2010. Methane-rich fluid evolution of the Baogutu porphyry Cu–Mo–Au deposit, Xinjiang, NW China. *Chem. Geol.* 275, 78–98.
- Sillitoe, R.H., 2010. Porphyry copper systems. *Econ. Geol.* 105, 3–41.
- Sterner, S.M., Hall, D.L., Bodnar, R.J., 1988. Synthetic fluid inclusions. V: Solubility relations in the system NaCl–KCl–H<sub>2</sub>O under vapor-saturated conditions. *Geochim. Cosmochim. Acta* 52, 989–1005.
- Sun, Q., 2009. The Raman OH stretching bands of liquid water. *Vib. Spectrosc.* 51, 213–217.
- Sun, W.D., Huang, R.F., Li, H., Hu, Y.B., Zhang, C.C., Sun, S.J., Zhang, L.P., Ding, X., Li, C.Y., Zartman, R.E., Ling, M.X., 2015. Porphyry deposits and oxidized magmas. *Ore Geol. Rev.* 65, 97–131.
- Sun, W.D., Liang, H.Y., Ling, M.X., Zhan, M.Z., Ding, X., Zhang, H., Yang, X.Y., Li, Y.L., Ireland, T.R., Wei, Q.R., Fan, W.M., 2013. The link between reduced porphyry copper deposits and oxidized magmas. *Geochim. et Cosmochim. Acta* 103, 263–275.
- Taghinejad, A., 2012. Petrology, alteration and copper mineralization in Keder area, Shahr-e-babak, Kerman province. M.Sc thesis. Islamic Azad University.
- Taghipour, N., Aftabi, A., Mathur, R., 2008. Geology and Re–Os geochronology of mineralization of the Miduk porphyry copper deposit. *Iran. Resour. Geol.* 58, 143–160.
- Tattitch, B.C., Candela, P.A., Piccoli, P.M., Bodnar, R.J., 2015. Copper partitioning between felsic melt and H<sub>2</sub>O–CO<sub>2</sub> bearing saline fluids. *Geochim. Cosmochim. Acta* 148, 81–99.
- Verdel, C., Wernicke, B.P., Hassanzadeh, J., Guest, B., 2011. A Paleogene extensional arc flare-up in Iran. *Tectonics* 30, 1–20.
- Wang, D., Bi, X., Lu, H., Hu, R., Wang, X., Xu, L., 2018. Fluid and melt inclusion study on mineralized and barren porphyries, Jinshajiang-Red River alkali-rich intrusive belt, and significance to metallogenesis. *J. Geochem. Explor.* 184, 28–39.
- Wang, R., Richards, J.P., Hou, Z., Yang, Z., Dufrane, A., 2014. Increased magmatic water content—the key to oligo-miocene porphyry Cu–Mo ± Au formation in the eastern gangdese belt, Tibet. *Econ. Geol.* 109, 1315–1339.
- Wang, Y.H., Zhang, F.F., Li, B.C., 2017. Genesis of the Yandong porphyry Cu deposit in eastern Tianshan, NW China: evidence from geology, fluid inclusions and isotope systematics. *Ore Geol. Rev.* 86, 280–296.
- Wang, Y.H., Zhang, F.F., Liu, J.J., Que, C.Y., 2016. Genesis of the Fuxing porphyry Cu deposit in Eastern Tianshan, China: evidence from fluid inclusions and C–H–O–S–Pb isotope systematics. *Ore Geol. Rev.* 79, 46–61.
- Wilkinson, J.J., 2001. Fluid inclusions in hydrothermal ore deposits. *Lithos* 55, 229–272.
- Williamson, B.J., Herrington, R.J., Morris, A., 2016. Porphyry copper enrichment linked to excess aluminium in plagioclase. *Nat. Geosci.* 9, 237–241.
- Wu, S., Zheng, Y., Geng, R., Jin, L., Bao, B., Tan, M., Guo, F., 2017. Geology, fluid inclusion and isotope constraints on ore genesis of the post-collisional Dabu porphyry Cu–Mo deposit, Southern Tibet. *Ore Geol. Rev.* 89, 421–440.
- Yang, X.M., 2012. Sulphur solubility in felsic magmas: Implications for genesis of intrusion-related Gold Mineralization. *Geosci. Can.* 39, 17–32.
- Yang, Y.F., Chen, Y.J., Pirajno, F., Li, F., 2015. Evolution of ore fluids in the Donggou giant porphyry Mo system, East Qinling, China, a new type of porphyry Mo deposit: evidence from fluid inclusion and H–O isotope systematics. *Ore Geol. Rev.* 65, 148–164.
- Yu, J., Li, N., Shu, S.P., Zhang, B., Guo, J.P., Chen, Y.J., 2017. Geology, fluid inclusion and H–OS isotopes of the Kuruer Cu–Au deposit in Western Tianshan. *Ore Geol. Rev.* Xinjiang, China. <https://doi.org/10.1016/j.oregeorev.2017.07.016>.
- Zarasvandi, A., Liaghat, S., Lentz, D., Hossaini, M., 2013. Characteristics of mineralizing fluids of the Darreh-Zerreshk and Ali-Abad porphyry copper deposits, Central Iran, determined by fluid inclusion microthermometry. *Resour. Geol.* 63, 188–209.
- Zarasvandi, A., Rezaei, M., Raith, J.G., Lentz, D.R., Azimzadeh, A.M., Pourkaseb, H., 2015a. Geochemistry and fluid characteristics of the Dalli porphyry Cu–Au deposit, Central Iran. *J. Asian Earth Sci.* 111, 175–191.
- Zarasvandi, A., Rezaei, M., Raith, J.G., Pourkaseb, H., Asadi, S., Saed, M., Lentz, D.R., 2018. Metal endowment reflected in chemical composition of silicates and sulfides of mineralized porphyry copper systems, Urumieh-Dokhtar magmatic arc, Iran. *Geochim. et Cosmochim. Acta* 223, 36–59.
- Zarasvandi, A., Rezaei, M., Sadeghi, M., Lentz, D., Adelpour, M., Pourkaseb, H., 2015b. Rare earth element signatures of economic and sub-economic porphyry copper systems in Urumieh-Dokhtar Magmatic Arc (UDMB), Iran. *Ore Geol. Rev.* 70, 407–423.
- Zhong, J., Chen, Y., Pirajno, F., Chen, J., Li, J., Qi, J., Li, N., 2014. Geology, geochronology, fluid inclusion and H–O isotope geochemistry of the Luoboling Porphyry Cu–Mo deposit, Zijinshan Orefield, Fujian Province, China. *Ore Geol. Rev.* 57, 61–77.